1	How Shrinkage of Lake Chad Affects the Local Climate
2	
3	
4	
5	Siyu Zhao ¹ , Kerry H. Cook ¹ , Edward K. Vizy ¹
6	
7	¹ Department of Geological Sciences, University of Texas at Austin, Austin, TX, USA
8	
9	
10	
11	Published in Climate Dynamics
12	August 12, 2022
13 14 15 16	This preprint has not undergone any post-submission improvements or corrections. The Version of Record of this article is published in Climate Dynamics, and is available online at https://doi.org/10.1007/s00382-022-06597-3 The sitution for this great is as full year.
18 19 20 21 22	The citation for this work is as follows: Zhao, S., K.H. Cook, and E.K. Vizy 2023: How shrinkage of Lake Chad affects the local climate. <i>Clim. Dyn.</i> , 61, 595-619. https://doi.org/10.1007/s00382-022-06597-3
23 24	Corresponding author address: siyu_zhao@utexas.edu

Abstract

25

26

27

28

29

30

31

32

33

34

35

36

37

38

39

40

41

42

Convective-permitting ensemble simulations are used to understand how areal changes of Lake Chad affect precipitation. Shrinkage of Lake Chad from about 25,000 km² to its current size (~1300 km²) increases rainfall over the lake basin in the afternoon. Reduced precipitation over a large lake is associated with a shallow planetary boundary layer, which decreases the likelihood of triggering convection by turbulence and weakens the vertical moisture mixing. As a result, the large lake does not act as a moisture source for afternoon convection, but lessens the low to mid-level humidity leading to a more stable daytime environment. Daytime lake breezes also act to inhibit convection over the large lake by inducing low-level moisture divergence and subsidence. During the recession to a small lake, Lake Chad is partially replaced by wetlands which also reduce local afternoon rainfall but not to the same extent as the large lake. This effect is primarily associated with anomalous subsidence and cooler surface temperatures over the wetlands than over the adjacent land during the day. Boundary layer heights over the wetlands are much higher than over the large lake, accounting for the wetlands' weaker effect in suppressing daytime rainfall. Loss of Lake Chad and adjacent wetlands impacts the local and mesoscale climate through modification of the spatial area influenced by daytime lake/wetland breezes. The rainfall response to the circulation perturbation of the lake/wetlands can be overlooked in models with cumulus convective parameterization.

43

44

45

Keywords: lake breezes, wetlands, Lake Chad, West Africa, Sahel, convective permitting modeling

1 Introduction

46

47

48

49

50

51

52

53

54

55

56

57

58

59

60

61

62

63

64

65

66

67

Lake Chad is a endorheic lake in West African Sahel (Leblanc et al. 2003; UNEP 2006; Bouchez et al. 2016). It is a vital water source for millions of people (Sarch and Birkett 2000; Okpara et al. 2016). Observations (Lemoalle et al. 2012; Onamuti et al. 2017; Pham-Duc et al. 2020) indicate that the lake area has decreased by over 90% since the 1970s in response to the changing climate and the increased water demand by the growing population. The reduction in lake area has adversely affected the ecosystem, fishing production and livelihood of local communities (UNEP 2006; Ngounou 2009; Onuoha 2009; Okpara et al. 2016; Yunana et al. 2017; Soboyejo et al. 2021). It is not completely understood how the reduced lake size has affected the regional climate, but such knowledge is crucial to improve future climate prediction in this area. The purpose of this study is to understand how the shrinkage of Lake Chad influences the local climate. Convective-permitting (CP) modeling is carried out at 3-km resolution to simulate past, present and future scenarios over the Lake Chad region. CP simulations have advantages in better representing small-scale processes, the diurnal cycle of rainfall and soil moistureprecipitation feedbacks than models with parameterized convection (Hohenegger et al. 2009; Kendon et al. 2012; Taylor et al. 2013; Prein et al. 2015; Finney et al. 2019). Thus, this will help us to better understand how changes in lake size can influence the circulation and precipitation in this region. Section 2 reviews background on Lake Chad as well as climate effects of lakes and wetlands. Section 3 describes the datasets, model configuration, experiment design and analysis tools. Results are presented in Sect. 4, and conclusions are drawn in Sect. 5.

68

2 Background

69

70

71

72

73

74

75

76

77

78

79

80

81

82

83

84

85

86

87

88

89

90

91

In the 1960s, Lake Chad had an area of about 18,000 - 25,000 km² (Crétaux and Birkett 2006; Lemoalle et al. 2012; Pham-Duc et al. 2020). Its surface area has decreased by over 90% since the 1970s, due to agricultural irrigation use and persistent droughts (Coe and Foley 2001; Lemoalle 2004; Onamuti et al. 2017; Zhu et al. 2019). Even with the recovery of the Sahel rainfall since the 2000s (Janicot and Kamga 2015; Nicholson et al. 2018; Biasutti 2019; Cook and Vizy 2019), the lake's bathymetry (Gao et al. 2011) and dam construction (Onamuti et al. 2017) are hindering restoration of the lake size. Presently, Lake Chad includes a southern and a northern basin divided by shoals, as well as an archipelago region (Carmouze and Lemoalle 1983; Lemoalle et al. 2012). The lake depth is about 2-4 and 4-8 m in the southern and northern basin, respectively (Odada et al. 2005). The southern basin is connected with the Chari-Logone River (Fig. 1), which is a major water input into the lake. If the river input is sufficient, water spills over the shoals and into the northern basin. The Komadugu-Yobe River directly discharges to the northern basin, but its inflow (0.44 km³/yr in 1983-2000) is smaller than that of the Chari-Logone River (19.4 km³/yr), as reported by Leblanc et al. (2011). The area of Lake Chad shows distinct seasonal and inter-annual variability (Lemoalle 2005). The local wet season occurs in boreal summer, but it takes time for water to drain into the lake basins. Thus, the water level in the southern basin is lowest in the boreal summer and highest in December (Leblanc et al. 2011). Dependent on whether and how much water spills into the northern basin, the northern pool can remain wet year around or dry up for several months to a whole year in extreme circumstances. Dry periods in the northern basin occurred in

every year of 1975-1998 and 2005-2012 (Lemoalle et al. 2012; Pham-Duc et al. 2020). The

present lake area is estimated to be between 876-5800 km² (Birkett 2000; Zhu et al. 2017; Onamuti et al. 2017; Buma et al. 2018; Pham-Duc et al. 2020), which is about 77-96% smaller than its size in the 1960s.

Few studies have focused on how Lake Chad affects the regional precipitation. Lauwaet et al. (2012) simulates three Lake Chad scenarios where there is a large/small or no lake, using a regional atmospheric model with cumulus convection and a 15-km spatial resolution. Restoration of Lake Chad does not induce a widespread precipitation increase over their model domain in boreal summer, but more rainfall is generated over the eastern side of the large lake compared with the small-lake experiment. They suggest that the higher rainfall to the east of the large lake is associated with enhanced evaporation over the lake. The low-level air is moistened by the lake and transported eastward by the prevailing low-level flow, enhancing convective systems east of Lake Chad. The large lake can also slow down the propagation of a typical mesoscale convective system (MCS) passing over it (Lauwaet et al. 2012), but this effect depends on lake temperatures and the time of the day and requires further study.

Taylor et al. (2018) also observe a weakening of storms as they traverse across the Lake Chad and the adjacent wetlands. However, they suggest that the afternoon convection is suppressed over the lake and wetland area, presumably due to daytime lake/wetland breezes. This is not consistent with precipitation difference between Lauwaet et al.'s (2012) large-lake and the small-lake experiments. Taylor et al. (2018) suggest that this difference may be associated with the convective parameterization in Lauwaet et al.'s (2012) model, as parameterized convection tends to predict positive feedbacks between soil moisture and precipitation (Taylor et al. 2013) in contrast to the observations (Taylor et al. 2012) and CP modeling results (Hohenegger et al. 2009; Taylor et al. 2013).

As indicated by the above studies, there are two competing mechanisms that lakes or wetlands interact with the overlying atmosphere to influence the local rainfall (Findell and Eltahir 2003a, b; Ek and Holtslag 2004; Diallo et al. 2018). The first is a thermodynamic mechanism, where the wetter surface affects the low-level moisture and the environmental instability over and near the area (Taylor et al. 1997; Taylor and Lebel 1998). The second is a dynamic mechanism, where the wetter surface perturbs circulation due to temperature and roughness contrasts between the area and the surrounding land (Emori 1998; Samuelsson and Tjernström 2001; Koseki and Mooney 2019; Woodhams et al. 2019). Lakes also affect the planetary boundary layer height (PBLH) (Li et al. 2018; López-Espinoza et al. 2019).

Due to different atmospheric conditions and the competing mechanisms, the influence of lakes or wetter surfaces (such as wetlands, wetter soil surfaces, irrigated areas and forests) on precipitation can be either positive (Segal et al. 1998; Clark et al. 2004; Thiery et al. 2015; Diallo et al. 2018) or negative (Segal et al. 1989; Rabin et al. 1990; Cheng and Cotton 2004; Negri et al. 2004; Mohamed et al. 2006; Taylor and Ellis 2006; Prigent et al. 2011; López-Espinoza et al. 2019). Most studies suggest that the effects on precipitation are locally restricted over lakes or wetter surfaces (Mohamed et al. 2005; Lauwaet et al. 2012; Thiery et al. 2015), while others infer influence over a larger region via long-lived storms (Taylor 2010; Taylor et al. 2018).

While the discussion above suggests that changes in Lake Chad's size can be a potentially important factor for modifying local/regional climate and rainfall, it is not completely clear to what extent and how influential it will be. Our study seeks to improve our understanding of this relationship.

3 Methodology

a. Experimental design

High resolution CP simulations using the National Center for Atmospheric Research (NCAR) Weather Research and Forecasting Model Version 4.1.3 (WRF; Skamarock et al, 2019) are utilized. Figure 1a shows the model configuration of triple-nested domains using one-way nesting. The outer domain has a resolution of 27 km. Its lateral boundaries are set far from Lake Chad to reduce influence from the prescribed lateral boundary conditions. Imbedded in the 27-km domain are 9-km and 3-km domains. All three domains have 43 vertical levels, with the top of atmosphere at 10 hPa. The model time steps are 90, 30 and 10 s and model output is saved every 3, 3 and 1 hour for the 27-km, 9-km and 3-km domains, respectively.

Convective parameterization is disabled in the 3-km domain. The coarser domains use the Kain-Fritsch cumulus convective scheme (Kain 2004). Other physical parameterizations are the same across all three domains. These include New Thompson et al. microphysics (Thompson et al. 2008), RRTM longwave radiation (Mlawer et al. 1997), Dudhia shortwave radiation (Dudhia 1989), Revised MM5 surface layer (Jiménez et al. 2012), Yonsei University planetary boundary layer (Hong et al. 2006) schemes and 4 layer Unified Noah Land Surface Model (Chen and Dudhia 2001). These choices are based on regional model applications that simulate a realistic African climate (Vizy and Cook 2009, 2018, 2019; Laing et al. 2012; Vizy et al. 2013; Crétat et al. 2015).

Based on other CP modeling studies (Hutchinson 2009; Jeworrek et al. 2019), an adaptive positive definite 6th order horizontal diffusion damping is applied in the 27-km/9-km/3-km domain to improve model stability, with coefficients of 0.2/0.3-0.35/0.3-0.4, respectively. An adaptive model time step approach is also applied, with time steps in the three domains occasionally halved.

Four experiments are carried out, referred to as Small-Lake, Large-Lake, Wetland, and Large-Lake-II (Table 1). Figure 1b presents the land use specification in the 3-km domain of Small-Lake, in which Lake Chad is small and surrounded by herbaceous wetlands that dry out through August. This environment represents recent years that are anomalously warm, and it is a possible future scenario with the wetlands lost.

Several default parameters in WRF are modified for the Small-Lake experiment according to observations. These include selecting the alternative set of land use categories based on USGS land-cover classification, increasing the lake area to 1296 and 1314 km² for the 9-km and 3-km domains, changing the 'Barren' land surrounding Lake Chad to 'Herbaceous Wetland' (Lemoalle et al. 2012; Tappan et al. 2016; Buchhorn et al. 2020), modifying 'Water' near the lake to 'Clay Loam' (estimated using SoilGrids250m 2.0 (Batjes et al. 2017)), and boosting the greenness fraction over the wetlands and the area at 13.5°N and 13.9°E to the median value over the wetlands from the 1999-2019 1-km Copernicus Global Land Service Fraction of Absorbed Photosynthetically Active Radiation (FAPAR) v2 (Copernicus Service information, 2022). 'Herbaceous Wetland' has relatively low albedo, high soil moisture availability and high thermal inertia compared with other land use types (Jiménez-Esteve 2016).

In the Large-Lake experiment (Fig. 1c), the wetland area stippled in Fig. 1b is specified as a lake. The area of Lake Chad is enlarged to 24921 km² in the 3-km domain. It represents the situation in the 1960s and recent during years with large river input.

The Wetland experiment (Fig. 1d) includes the small Lake Chad area as in Small-Lake (Fig. 1b), but soil moisture over the wetlands region is kept relatively high at 58% saturated (constant at 0.2697 m³/m³). This configuration is most similar to recent years, on average. Surface lake temperatures over Lake Chad in the Wetland simulation are corrected from Small-

Lake (shown later). Surface specifications over the wetland area are also modified from Small-Lake to reduce heterogeneity out of scope of the study. Isolated points of other land use types are merged into wetlands. Greenness fraction is boosted to the August mean FAPAR value over the wetland area for all twelve months.

In the Large-Lake-II experiment (Fig. 1e), the wetland region in Fig. 1d is specified as a lake. The configuration is similar to Large-Lake, but the prescribed surface temperatures are adjusted both in the diurnal cycle and in magnitude from Large-Lake to better represent the observation (Figure 2; discussed later). Due to the inclusion of isolated points at the edges, lake area in Large-Lake-II is slightly larger than that in Large-Lake in the 3-km domain. Thus, Large-Lake-II serves as the comparative experiment to Wetland and a sensitivity test to the Large-Lake simulation.

Small-Lake and Large-Lake both include 5 ensemble members, while Wetland and Large-Lake-II have 3 ensemble members. Each simulation is run from 00Z 01 July to 00Z 01 September. The first month is used for model spin-up and is discarded. August, the peak of the local rainy season, is chosen as the analysis period. The model is unstable during 12Z 14-15 August 2017 in Large-Lake, and output for these two days is discarded.

Initial and 3-hourly lateral boundary conditions for the 5 ensemble members of Small-Lake and Large-Lake are derived from the 0.25° ERA5 reanalysis (Copernicus Climate Change Service 2017) for 2013 – 2017. Wetland and Large-Lake-II utilize data from 2013 to 2015. The same soil moisture is used to initialize Small-Lake and Large-Lake, calculated from the 2007 – 2019 average in ERA5 at 00Z 01 July and increased from 0.05-0.09 to 0.2 m³/m³ over the wetlands. 0.2 m³/m³ approximates the quasi-equilibrated soil moisture in the top two soil layers in a 45-day trial simulation. The settings of the trial simulation are similar to Small-Lake, but the

soil type over the wetland area is 'Clay'. Soil moisture at 00Z 01 September from the Small-Lake 2013 simulation is used to initiate Wetland and Large-Lake-II.

Sea Surface temperatures are prescribed every 3 hours using the 0.05° daily Operational Sea Surface Temperature and Sea Ice Analysis (OSTIA; Donlon et al. 2012) climatology for 2007 – 2019, smoothed with a 30-day running mean. OSTIA does not offer data over Lake Chad so five other datasets are examined including SUMET, ERA5, and ARC-Lake (Figure 2a; Table 2). SUMET is used to prescribe a uniform lake surface temperature that includes a diurnal cycle over Lake Chad due to its high resolution.

Figure 2b shows that prescribed Lake Chad lake surface temperatures in WRF are discrete and update every 3 hours. There is an erroneous one-hour delay in the temperature diurnal cycle in the 3-km domain of Small-Lake and Large-Lake, which was adjusted for in the Wetland and Large-Lake-II simulations. This temporal displacement also occurs, and is corrected, for sea surface temperatures but differences are minor, with a maximum difference of 0.07 K.

Figure 2c shows that the 3-km domain of Small-Lake simulates a diurnal surface temperature maximum 6.57 K higher than SUMET averaged over the wetland area (stippled in Fig. 1b). It is comparable to 4 out of 25 years in the SUMET record (not shown). By contrast, the coarser domains produce lower wetland temperatures. Through a surface energy budget analysis (not shown), the lower temperatures are related to enhanced evaporation and soil moisture over the wetlands due to higher precipitation and cumulus convection. Based on this, the Wetland experiment is designed with relatively high soil moisture over the wetlands, generating a diurnal temperature maximum 1.97 K higher than SUMET. The 58% soil saturation is determined by

trial and error. The 2013 ensemble member is run with 70% soil saturation over the wetlands forthe first 11 days.

231

232

- b. Analysis datasets and tools
- Multiple precipitation datasets are used to evaluate model simulations (Table 3). The conservation of water equation for the atmosphere is used to understand the diurnal cycle of specific humidity, q. The time rate change of q can be written as the sum of divergence of moisture flux, evaporation, e, condensation, c, and turbulence due to sub-grid and sub-hourly intensities, *T*, according to:

238
$$\frac{\partial q}{\partial t} = -\nabla_h \cdot (q\vec{v}) - \partial_p(\omega q) + e - c + T, \tag{1}$$

where \vec{v} is horizontal wind velocity and ω is vertical p-velocity. e - c + T is computed as a residual. Integrating Eqn.1 vertically and averaging over a period of time gives the atmospheric column moisture budget (Lenters and Cook 1995; Seager and Henderson 2013):

$$\langle \frac{\partial q}{\partial t} \rangle = -\langle \nabla_h \cdot (q\vec{v}) \rangle + ET - P + R, \tag{2}$$

- where $\langle \ \rangle \equiv -\frac{1}{g\rho_w} \int_{p_s}^{100\;hPa} dp, \ \rho_w$ is the density of water, ET is evapotranspiration and P is
- precipitation. R is the residual that includes a boundary term, $-\frac{1}{g\rho_w}\omega_s q_s$, column-integrated
- 245 turbulence, $\langle T \rangle$, and numerical error, ε , according to:

$$R = -\langle \partial_p(\omega q) \rangle + \langle T \rangle + \varepsilon = -\frac{1}{g\rho_w} \omega_s q_s + \langle T \rangle + \varepsilon, \tag{3}$$

- 247 where subscript s denotes surface values.
- Moist static energy (MSE) is used to analyze stability of the atmosphere. MSE is defined as the sum of thermal, potential and latent energy of the air parcel according to:

$$MSE = C_p T + \Phi + L_v q, \tag{4}$$

where C_p is the specific heat capacity of dry air at constant pressure (1004 J kg⁻¹ K⁻¹), T is temperature, Φ is geopotential, and L_v is the latent heat of vaporization of water (2.5 × 10⁶ J kg⁻¹).

4 Results

a. Model Evaluation

Figure 3 presents rainfall observations and the simulated precipitation in the three domains of Small-Lake during August. In IMERG (Fig. 3a), higher rainfall (above 7 mm/day) is present near 10°N across West and Central Africa. Local maxima exceeding 10 mm/day occur over topography, including the Guinea Highlands, the Cameroon Highlands and the Jos Plateau.

CMORPH and CHIRPS2 have rainfall distributions similar to IMERG, although there are some differences. For example, CMORPH (Fig. 3b) does not capture the rainfall maxima over the Guinea Highlands (10°N, 10°W) and the Jos Plateau (10°N, 10°E), but it produces higher rainfall over the Cameroon Highlands (7°N, 11°E). CHIRPS2 (Fig. 3c) has an additional rainfall maximum over the Bongo Massif (9°N, 22°E).

In the coarser domains of Small-Lake (Figs. 3d - e), precipitation is unrealistically high over West and Central Africa. In the 3-km domain (Fig. 3f), with resolved convection, the average rainfall is similar to the observations. Large-scale rainfall in the Wetland experiment is very similar to that in Small-Lake (not shown).

Figure 4 shows 875-hPa and 600-hPa atmospheric circulation and moisture fields in the ERA5 reanalysis and the 3-km domain of Small-Lake. ERA5 indicates that there is a sharp meridional gradient in low-level specific humidity around 18°N during August at 875 hPa, with geopotential decreasing from southwest to northeast (Fig. 4a). Low-level winds are

southwesterly or westerly over the West African Sahel, and converge with northerlies across the Sahara near 18°N. The meridional gradient of moisture is smaller at 600 hPa (Fig. 4b), partially because the dry air over the western Sahara does not extend this high into the troposphere.

Geopotential generally increases to the north, with the African Easterly Jet present at 10 - 17°N across the Central and West Africa.

The atmospheric fields from Small-Lake are similar to those from ERA5. At 875 hPa (Fig. 4c) the model captures the meridional gradient of moisture. However, the simulated specific humidity is generally lower than ERA5 and the boundary between the moist and dry air is located further south, roughly 2° latitude at 10 - 25°E. The simulated geopotential is higher over the Guinean coast and the eastern Sahara than in ERA5. This is associated with further invasion of northeasterlies from the Sahara in the model.

At 600 hPa (Fig. 4d), the African Easterly Jet is well represented by Small-Lake. The model is able to replicate the August geopotential gradient over the Sahel and western Sahara. The simulated moisture is lower over the Guinean coast and higher around South Sudan (10°N, 30°E) compared with ERA5. The atmospheric fields simulated by Wetland are similar to those of Small-Lake (not shown).

Model evaluation close to Lake Chad is more limited because observational datasets do not provide consistent rainfall estimates. IMERG (Fig. 5a), based on satellite microwave and infrared estimates, presents a rainfall maximum over the wetlands and the lake. However, the rainfall enhancement over the wetlands/lake can be associated with the passive microwave algorithm overestimating precipitation over inland water bodies (Tian and Peters-Lidard 2007; Taylor et al. 2018). The infrared-only dataset in IMERG does not produce similar rainfall enhancement over Lake Chad and adjacent wetlands (not shown). While the input for CMORPH

(Fig. 5b) is satellite microwave measurements as well, CMORPH indicates suppressed rainfall activity over the wetlands (also in Figure 9 of Taylor et al., 2018) and a south-to-north precipitation gradient.

Input for CHIRPS2, TARCART, ARC2 and PERSIANN is mostly satellite infrared data incorporated/calibrated with ground-based observations. CHIRPS2 (Fig.5c) places a rainfall minimum of 1 mm/day over the wetlands, but this rainfall minimum is not directly recorded by in-situ data incorporated in CHIRPS2. Similar to CHIRPS2, TARCAT (Fig. 5d) indicates stronger rainfall suppression over the wetlands than CMORPH. However, similar calibration approaches are used in CHIRPS2 and TARCAT (Funk et al. 2015) helping to explain their consistency. ARC2 (Fig. 5e), PERSIANN (Fig. 5f) and TMPA that preceded IMERG (not shown) indicate a south-to-north rainfall gradient similar to CMORPH (Fig. 5b). Overall, most datasets imply that Lake Chad and the surrounding wetlands either suppress or have no obvious influence on the local rainfall. In-situ measurements are required for a more complete validation.

Figure 5g presents the ensemble mean rainfall near Lake Chad in the 3-km domain of Small-Lake. It shows a meridional precipitation gradient and rainfall magnitudes that are roughly 2 mm/day less than the observations. Lauwaet et al. (2012) also reported rainfall is underestimated over the region in their model.

Figure 5h shows the ensemble mean rainfall in the 3-km domain of Wetland. The spatial distribution and magnitudes of precipitation are similar to that of Small-Lake, except for the lower rainfall amounts over the northern part of the wetlands.

Few rainfall observations resolve the diurnal cycle near Lake Chad. Thus, despite the possible biases of microwave-based precipitation estimates over inland water bodies (Tian and Peters-Lidard 2007; Taylor et al. 2022), IMERG, CMORPH and TMPA are used to evaluate the

simulated August rainfall diurnal cycle area-averaged over Lake Chad (Figures 6a-c). The infrared-only rainfall dataset in IMERG is included as a supplementary (dashed lines). The averaging regions for the observational datasets are interpolated from the area of Lake Chad in the 9-km or 27-km domains of Small-Lake.

Similar to Fig. 5, the rainfall observations do not agree well with each other over the lake (Fig. 6a). While IMERG indicates a bimodal diurnal cycle with peaks in the early morning and late afternoon, the infrared-only rainfall dataset in IMERG shows a major afternoon peak of approximately 14 mm/day. CMORPH shows one rainfall peak in the early afternoon. TMPA rainfall has similar diurnal range to CMORPH at 3-8 mm/day, but with a bimodal diurnal cycle as in the full IMERG product.

The simulated rainfall diurnal cycle over the lake has several peaks in the 3-km domain of the Small-Lake ensemble mean (Fig. 6b). Rainfall events tend to be sporadic over the lake in the model. For example, the peaks at 09Z, 14Z and 23Z result from individual rainfall events that have mean intensity exceeding 25 mm/day over Lake Chad (not shown). The simulated rainfall is lower than observed. The coarser domains generate higher rainfall than the 3-km domain throughout the day, with rainfall peaks in the early morning and early afternoon.

The 3-km domain of Wetland shows lower rainfall rates than the observations and different rainfall timing from Small-Lake (Fig. 6c). However, this timing difference is likely not caused by the one-hour shift in the prescribed diurnal lake temperatures. This conclusion is later verified in the comparison between the two large-lake simulations. The coarser domains show especially high rainfall peaks in the early morning.

Figures 6d-f present the observed and simulated rainfall diurnal cycle over the wetlands, the area of which is shown in Fig. 1b. Again, the averaging regions for the observational datasets

are interpolated from the area in Small-Lake. All three observational datasets produce a unimodal diurnal cycle (Fig. 6d). CMORPH and TMPA are similar to each other, with one rainfall peak of roughly 8 mm/day around 15Z. IMERG produces higher rainfall throughout the day, with an afternoon peak of 10 mm/day. The infrared-only dataset shows lower (higher) rainfall amount in the morning (afternoon) than the full product of IMERG. The better agreement among these datasets over the wetlands than over the lake is at least partly related to having a larger averaging region. The observed rainfall is of similar magnitudes over adjacent land areas (12.5°N-14.5°N, 12°E-13°E and 12.5°N-14.5°N, 15.5°E-16.5°E; not shown). The rainfall peaks are later over the adjacent land areas, at 15Z-18Z and roughly 18Z-21Z, respectively.

The rainfall diurnal cycle in the 3-km domain of Small-Lake is similar to the observations despite its lower intensity (Fig. 6e). Out of the 34 rainfall events with peak hours at 14Z-15Z and rainfall rates exceeding 1mm/day over the wetlands, 29 are generated over the wetlands and they account for 51% of the total precipitation (not shown). Some of these storms dissipate locally, while the rest develop into or merge with MCSs and propagate away from the lake. In contrast to the 3-km domain, the coarser domains do not capture the rainfall diurnal cycle, and simulate high rainfall peaks at 12Z.

The rainfall diurnal cycle in the 3-km domain of Wetland misses the afternoon peak shown in the observations (Fig. 6f). There are only 9 rainfall events that exceed 1mm/day over the wetlands and peak at 14Z-15Z (not shown). Most of them are generated over or in close vicinity to the wetlands. The coarser domains generate a high rainfall peak at 12Z. This and Fig. 6e illustrate that parameterized convection can overestimate tropical rainfall and predict peak intensity at mid-day over land.

In conclusion, Small-Lake and Wetland are able to represent the large-scale precipitation and circulation well in the 3-km domain. By contrast, the coarser domains overproduce rainfall over West and Central Africa. On smaller space scales close to Lake Chad and on the diurnal time scale, the observations are more limited. With IMERG as an outlier, three of the seven datasets show suppressed rainfall over the wetlands adjacent to Lake Chad, while the other three present a northward precipitation decline over the region. The simulations display a similar rainfall distribution, but at lower magnitudes. While the simulated rainfall diurnal cycle in the model is by no means perfect, the contrast between the 3-km and the coarser domains clearly illustrates the added value of explicitly resolving convection. Thus, it is still useful to analyze the small-scale features of the simulated rainfall and their differences in the various experiments as results from 3-km domain are physically produced by explicitly solving governing equations, allowing us to understand the mechanisms behind the differences in rainfall between the experiments. Furthermore, the good representation of large-scale precipitation and circulation adds credentials to the simulations. Additionally, observations can be plagued by resolution issues and lack of observing stations over the Lake Chad region.

380

381

382

383

384

385

386

387

365

366

367

368

369

370

371

372

373

374

375

376

377

378

379

b. Effects of a Large Lake

Figure 7 shows the August rainfall difference between Small-Lake and Large-Lake. Compared with Small-Lake, rainfall is 1-3 mm/day lower over the basin in Large Lake (Fig. 7a). This decrease in rainfall is statistically significant at the 95% level of significance over much of the lake basin. East of the lake rainfall increases with the presence of the large lake, however the areas of significant differences are not as robust in size. For the same reason, remote influences outside the basin of a large Lake Chad are not discernable in this simulation.

Figure 7b presents the rainfall diurnal cycle over the wetland area (stippled in Fig. 1b) in Small-Lake, Large-Lake, and Large-Lake-II. The wetland area is selected as the averaging region in this and the following analysis because the rainfall anomalies and modifications to the surface specifications are located there. Rainfall is significantly lower in the afternoon in the two large-lake simulations compared with Small-Lake.

The precipitation diurnal cycle is similar in the two large-lake experiments. The rainfall peak at 06Z in Large-Lake-II is associated with two intense storms so its presence is likely not a climatological difference. Aside from 06Z, Large-Lake and Large-Lake-II are similar. The comparison indicates that the issue with the one-hour shift in the diurnal cycle of lake temperature is not inducing a notable difference in the rainfall response.

The atmospheric stability is analyzed to understand the rainfall suppression over the large lake. Composites are made for dry and rainy hours (days), when precipitation averaged over the wetland area is less or greater than 1 mm/day.

Figure 8a shows the vertical profile dry composite of the Large-Lake minus Small-Lake difference in MSE and its terms (Eq. 4) at 15Z averaged over the wetland area. 15Z is representative of the daytime hours of 10Z-18Z. The atmosphere is more stable (unstable), if the slope of the MSE vertical profile anomalies is positive (negative). The lower troposphere (950-775 hPa) is more unstable in Large-Lake, while mid-levels (775-625 hPa) are more stable. The anomalous MSE is dominated by the moisture term until 400 hPa. Cooler lake temperatures induce a decrease in the thermal energy (C_pT) that partially cancels out the increase in latent energy. The more stable mid-level and the reduced moisture at 900-625 hPa do not favor convective development in Large-Lake.

Figure 8b is similar to Fig. 8a but for 00Z, representing nighttime conditions between 23Z-07Z. The lower troposphere is more unstable in Large-Lake primarily due to higher specific humidity levels. Magnitudes of the anomalies are smaller than those at 15Z. Similar daytime and nighttime conditions occur in the rainy-hour composites, but are present at 12Z-17Z and 20Z-01Z, respectively (not shown).

To understand the difference in potential stability, Figures 8c-d show the diurnal cycle of CIN at 950 hPa over the wetland area in Large-Lake and Small-Lake for the dry- and rainy-day composites. The 950-hPa CIN is higher in Large-Lake during the daytime in both dry- and rainy-day composites, inhibiting convective development. Note in the discussion that follows, notable differences between the dry and rainy composites identified will be pointed out and shown when relevant, however if the dry and rainy composites are similar, only the dry composite is shown for the sake of brevity.

Figures 9a-b show the diurnal cycle of specific humidity over the wetland area for the dry-day composites. In Small-Lake (Fig. 9a), the 925-hPa specific humidity reaches a maximum at 08Z, decreases until 16Z, and then increases again. The peak of the specific humidity during the daytime is later at higher levels (925-625 hPa). By contrast, the amplitude of the moisture diurnal cycle is small in Large-Lake above 850 hPa (Fig. 9b). Compared with Small-Lake, the specific humidity in Large-Lake is higher in the early morning at 925-775 hPa and lower in the afternoon at 825-625hPa. This is consistent with the differences in the latent energy shown in Fig. 8. The rainy composite specific humidity is higher over the wetland area at all times than the dry composites (not shown).

The atmospheric water balance (Eqn. 1) is used to understand differences in the moisture diurnal cycle between Small-Lake and Large-Lake. Figures 9c-d show the diurnal cycle of the

time rate change of specific humidity over the wetland area. In Small-Lake (Fig. 9c), the delay in the moisture diurnal cycle between 925 hPa and 800 hPa is clearly shown, as identified in Fig. 9a. In Large-Lake (Fig. 9d), the time rate of change of the specific humidity above 850 hPa is small. Moisture at 925-850 hPa decreases between 11Z and 19Z and increases between 20Z and 10Z. This is different from Small-Lake.

Figures 9e-f show the diurnal cycle of the moisture flux convergence over the wetland area. In Small-Lake (Fig. 9e), moisture flux convergence primarily accounts for the change of specific humidity at night but is small during the day. Thus, the moisture flux convergence does not explain the delay in the moisture diurnal cycle across different pressure levels. In Large-Lake (Fig. 9f), the moisture flux convergence dominates the moisture change throughout the day, which is especially large in the afternoon. This implies that different circulations influence moisture transport in the two experiments.

Figures 9g-h present the residual term over the wetland area. The residual term includes evaporation, condensation, turbulent transport of moisture and numerical error. The residual term dominates the moisture change during the daytime in Small-Lake (Fig. 9g). In Large-Lake (Fig. 9h), the residual term is small above 900 hPa and it partially balances out the divergence of moisture flux in Large-Lake at 925-900 hPa.

To understand the role of phase changes of water in the residual term, Figures 10a-b show the diurnal cycle of water in non-gas phases at 925-625 hPa over the wetland area for the dry-day composite. In Small-Lake (Fig. 10a), the non-gas water increases during the day at 800-625 hPa. This is associated with the formation of clouds (and hydrometeors in the rainy-day composite; not shown). However, the amount of condensed water is about 3 orders of magnitude less than the diurnal change of water vapor shown in Fig. 9. Although an afternoon peak of the

non-gas water does not occur in Large-Lake (Fig. 10b), this difference is small relative to that of the residual terms.

Turbulence can be generated thermally with the growth of boundary layer. To examine the effects of turbulent moisture transport, Figures 10c-d show the time and height when the daytime relative humidity is maximum at 925-625 hPa as well as the PBLH over the wetland area for the dry-day composite. In Small-Lake (Fig. 10c), the line of daytime maximum relative humidity that ranges from 56.2% to 63.0% aligns well with the PBLH. In other words, a pressure level tends to have its highest relative humidity around when it is first merges with the planetary boundary layer. The relative humidity at 725-650 hPa reaches the daytime maximum at about 15Z, implying the presence of turbulence above the defined PBLH. This can occur when the bulk Richardson number method in the numerical scheme underestimates the PBLH (Zhang et al. 2014; Bakas et al. 2020; Li et al. 2022). In Large-Lake (Fig. 10d), the PBLH does not reach 950 hPa and the daytime maximum relative humidity is lower than 56.3% above 900 hPa.

The time and height of daytime maximum relative humidity follow the growth of the PBLH in Small-Lake in the rainy-day composite, unlike in Large-Lake (not shown). However, the relative humidity is also high over the large lake in the rainy days. This is associated with the moisture brought by atmospheric circulation and rainfall systems.

The shallow PBLH is not only associated with low mid-level moisture over the large lake, but also with weakening a potential lifting mechanism for local storm genesis. Figures 11a-b show the PBLH and the level of free convection (LFC) over the wetland area in Small-Lake and Large-Lake. In the dry-day composite (Fig. 11a), the PBLH and the LFC are both lower over the large lake during the daytime. The PBLH ranges from 174 m to 2482 m in Small-Lake, and from 98 m to 303 m in Large-Lake. The LFC grows from 3907 m to 6901 m in Small-Lake

during the day, but shows small diurnal variation in Large-Lake (2421-2983 m). In both experiments, the PBLH is considerably lower than the LFC and vertical turbulent mixing within the boundary layer is not sufficient to lift an air parcel to a level of positive buoyancy on dry days.

Unlike the diagnostics examined before, the LFC in Small-Lake is significantly lower in the rainy-day composite (Fig. 11b) than in the dry-day composite. The PBLH approaches the LFC in Small-Lake in the early afternoon, favoring local storm genesis. By contrast, the PBLH in Large-Lake remains below the LFC throughout the day. Thus, vertical turbulent mixing cannot serve as a convection trigger over the large lake.

The growth of the PBLH is associated with entrainment and vertical motion at the top of the boundary layer (Eqn. 9.27 in Stull 2006). These factors are examined to understand why the PBLH is lower over the large lake than over the wetlands.

Figure 11c shows the sensible heat flux and the difference between the 700-hPa and the 950-hPa potential temperatures over the wetland area in Small-Lake and Large-Lake in the dry-day composites. These two diagnostics are chosen to approximate the entrainment rate, which measures the rate of air being drawn from the free atmosphere into the turbulent mixed layer (Stull 2006). Entrainment feeds the growth of the planetary boundary layer, which increases with the sensible heat flux and decreases with the strength of the capping inversion (estimated by the potential temperature difference here, the diurnal cycle of which is small above 700 hPa). Large-Lake produces lower sensible heat flux but stronger capping inversion than Small-Lake during the day. This leads to weaker entrainment over the large lake and contributes to the low PBLH.

Figure 11d shows the vertical p-velocity at the pressure level closest to the PBLH over the wetland area in Small-Lake and Large-Lake in the dry-day composites. Vertical motion at the

PBLH is downward in Large-Lake, contributing to the thinning of the planetary boundary layer over the large lake. The vertical motion is upward in Small-Lake, which thickens the boundary layer over the wetlands.

Figure 11e presents that the sensible heat flux is lower over the wetland area in Large-Lake compared with Small-Lake. To explore the reasons, three factors are analyzed according to the bulk aerodynamic formula (Fairall et al. 2003; Jiménez et al. 2012), including the surface wind speed, the ground-air temperature difference and the bulk coefficient. Figure 11f presents the 10-m wind speeds and the differences between the surface and 2-m temperatures over the wetland area in Small-Lake and Large-Lake in the dry-day composites. The temperature difference between the surface and the 2-m air is smaller in Large-Lake. This is related to cooler surface temperatures over the lake than over the wetlands (Fig. 2) and contributes to the lower sensible heat flux over the large lake. The higher surface wind speed in Large-Lake has the opposite but secondary effect.

Roughness length is approximately 0.20 over the herbaceous wetlands and 0.0001 over water bodies (not shown). This leads to lower efficiency (smaller bulk coefficients) for transferring sensible heat to the atmosphere over the lake than over the wetlands, and contributes to the lower sensible heat flux over the large lake.

To examine the circulation over and near Lake Chad, Figure 12a shows the 2-m temperature and 10-m wind in Small-Lake at 12Z for the dry-day composite, which excludes the direct impacts of storms on the circulation. Lake temperatures are cooler than the surroundings. Near the small lake, this induces divergent lake breezes imbedded in a background westerly/southwesterly flow field. Figure 12b presents the vertical cross section of zonal wind and vertical p-velocity at 12Z for the dry-day composite averaged over the latitudes of the small

lake. The longitudes of the small (large) lake are marked by light (dark) blue. There is subsidence of roughly 0.2 to 0.7 Pa/s at 950-800 hPa over the small lake. The subsidence lasts from 10Z to 17Z (not shown).

Figures 12c-d are similar to Figs. 12a-b but for Large-Lake. Compared with Small-Lake, lake breezes and low-level subsidence occur over a larger area. Figures 12e-f show circulation differences between the two experiments at 12Z. There are cooler temperatures, anomalously divergent winds and anomalous subsidence below 800 hPa over the wetland area. The subsidence and low-level divergence stabilize the afternoon atmosphere and transport drier air downward, helping to inhibit the development convective activity directly over the lake.

There is anomalous upward motion over the small-lake area in Fig. 12f, which indicates weaker subsidence in this region. To understand this, Figures 13a-b show the material accelerations of the 875-hPa vertical p-velocity in Small-Lake and Large-Lake at 12Z for the dry-day composite, with Fig. 13c presenting the anomalies. 875 hPa represent the lower levels. The material acceleration of vertical p-velocity is downward over the small lake and upward at the coasts (Fig. 13a). The acceleration is highest at the edge of the lake where the temperature contrast is the sharpest. Similarly in Large-Lake (Fig. 13b), the vertical acceleration is concentrated at the lake boundaries. Enlarging the lake size changes the locations of the strongest vertical acceleration (Fig. 13c), and further affects the spatial distribution of low-level subsidence during the growth of lake breezes (not shown). The changed locations of the strongest subsidence, as the lake is enlarged, are related to the weaker subsidence over the small-lake area shown in Fig. 12f.

No land breezes are identifiable in the dry-day composite (not shown), as the adjacent land cools to about the same temperature as the lake at night, minimizing the lake-land

temperature contrast. Surface winds are convergent over the lake at some night hours in the rainy-hour composites, but not necessarily with lake temperatures warmer than the surroundings. Surface winds are stronger over the lake than over the surroundings at night, likely due to the smoother lake surface.

To identify the moisture sources for precipitation, Figures 14a-d show the daily-mean differences of moisture budget terms (Eq. 2) between Large-Lake and Small-Lake ensemble means. The precipitation is lower over the larger lake (Fig. 14a), even though the evaporation is enhanced over the large-lake area (Fig. 14b). The horizontal moisture flux divergence increases at the coasts of the large lake (Fig. 14c). This is canceled out by the increase in the residual term (Fig. 14d) which likely consists of anomalies of the boundary term induced by different land-lake temperature and pressure contrasts with various lake areal sizes. The lower rainfall values over the large lake are primarily associated with the differences in the residual term. According to Eq. 3, the low-level subsidence due to lake breezes and the weaker turbulence with the lower PBLH are two potential reasons for the reduced moisture supply for precipitation over the large lake. The vertically-integrated time rate change of specific humidity is small when averaged over time (not shown).

In conclusion, rainfall is locally suppressed over the large lake compared with the small lake through two mechanisms. First, the planetary boundary layer is not as deep over the large lake than over the drying out wetlands. This makes the triggering of convection less likely during the day in association with weaker vertical turbulent mixing of moisture and enhanced low-level CIN. The weaker vertical mixing traps the moist air near the surface despite the enhanced evaporation over the large lake, resulting in less moisture at low to mid-levels over the large lake during the daytime. This further increases mid-level atmospheric stability and lessens

precipitation over the large lake. Second, lake breezes during the day induce low-level moisture divergence and subsidence over the large lake, inhibiting convection.

c. Effects of Wetlands

The Wetland experiment represents a transitional stage in the recession from a large Lake Chad to a small lake. The presence of wetlands potentially affects the local rainfall, but the effects and mechanisms can be different from the large lake. This is explored by comparing the Small-Lake, Wetland and Large-Lake-II simulations.

Figure 15a shows the ensemble-mean rainfall diurnal cycle in the three experiments over the wetland area. Wetland produces lower rainfall than Small-Lake in the afternoon over the wetland area. Although the ensemble-mean rainfall is higher in Wetland than that in Small-Lake in the early morning, the difference is not statistically significant and does not occur in every ensemble member (not shown). Rainfall in Wetland is higher than that in Large-Lake-II over the area for most of the day, but the difference is only statistically significant at 15Z (not shown). Overall, the wetlands reduce the local rainfall in the afternoon, but the effects are somewhat weaker than the large lake.

Analyses similar to Section 4b are carried out to understand the lower rainfall over the wetlands. Figure 15b shows the ensemble-mean PBLH in the three simulations over the wetland area. The PBLH in Wetland is lower than that in Small-Lake over the area but is much higher than the PBLH in Large-Lake. Thus, turbulence remains a possible trigger for convection and a mechanism for vertical moisture transport over the wetlands, supporting an environmental instability similarly or more favorable for convection than Small-Lake (not shown). The shallow PBLH, as one of the mechanisms for the large lake to suppress afternoon rainfall, does not apply

to the wetlands. Similarly, the enhanced CIN, as another way for the large lake to inhibit convection, does not occur over the wetlands (not shown).

Figure 15c presents the diurnal cycle of the 825-hPa vertical p-velocity over the wetland area in Small-Lake, Large-Lake-II and Wetland for the dry-day composite, excluding direct influence of storms. 825 hPa is representative of the low levels. The low-level vertical motion is upward over the area in Small-Lake, while subsidence occurs in Large-Lake-II and Wetland during the daytime. The subsidence is associated with lake breezes (Fig. 12) and wetland breezes, respectively. This is further related to the cooler surface temperatures over the lake/wetlands than over the drier land (Fig. 2c). However, the surface wind anomalies induced by the wetlands (not shown) are much weaker than those over the large lake (Fig. 12e), at roughly 0-2 m·s⁻¹. Overall, the afternoon rainfall suppression over the wetlands is related to the low-level subsidence and the cooler surface temperatures, which dominate over the PBLH mechanism.

5 Conclusions

Lake Chad is a small inland lake over the West African Sahel. It has shrunk by over 90% since the 1970s due to persistent droughts and increased withdrawal for agricultural use. The present lake size also varies seasonally and inter-annually. The purpose of this study is to use convective-permitting modeling to better understand how changes in Lake Chad's size affect precipitation, which is helpful for improving local/regional climate prediction in this area including a better understanding of past and future trends.

Four ensemble simulations for the month of August are carried out. Each experiment consists of five or three ensemble members and uses a triple nested (27-km/9-km/3-km) one-way

- nesting domain configuration. Convection is explicitly resolved in the 3-km domain. As summarized in Table 1, the experiments are as follows:
- The "Small-Lake" simulation represents anomalously warm years in the current climate and a possible future scenario. It includes a small Lake Chad surrounded by drying wetlands.
- In the "Large-Lake" simulation, the wetland area is replaced by lake water to represent the
 1960s' climatology, and also some recent years with anomalously high river input (although
 not necessarily high rainfall over the lake itself).
- "Wetland" is similar to Small-Lake but soil moisture over the wetlands is constrained at a higher value to represent a recent average year.
- "Large-Lake-II" is similar to Large-Lake but with adjusted lake temperatures as a sensitivity test.

The 3-km domains of the Small-Lake and Wetland simulations represent the observed large-scale precipitation and circulation well, with a southward rainfall gradient over the area that is consistent with three out of the seven observational datasets analyzed at high resolution. The coarser domains generate unrealistically high rainfall. The 3-km domain of Small-Lake captures the rainfall diurnal cycle over the wetlands. Although the 3-km domain of Wetland misses the afternoon rainfall peak over the wetland area, both convective-permitting domains contrast with the coarser domains that simulate high rainfall peaks in the early morning and early afternoon.

In Large-Lake, rainfall is suppressed over the large lake in the afternoon compared with Small-Lake. This is associated with a shallower PBLH over the large lake during the day which weakens the triggering of convection and vertical mixing of moisture by turbulence. Thus, even though evaporation is enhanced over the large lake, the low and mid-level atmosphere is drier

over the large lake, leading to higher mid-tropospheric stability. Daytime lake breezes also contribute to convective inhibition by inducing low-level divergence and subsidence, stabilizing the afternoon atmosphere and transporting drier air downward. Nighttime land breezes do not occur in this study, since the lake and adjacent land temperature contrast is minimal. Higher low-level CIN is another environmental factor limiting the triggering of convection.

A remote influence of the large lake on precipitation over West Africa is not detectable at statistical significance, even with five ensemble members. This relationship may warrant future attention, presumably in a study with more ensemble members.

The simulations show that, similar to the large lake, the wetlands also suppress local rainfall in the afternoon, but the effect is weaker. Lower rainfall over the wetlands is associated with low-level subsidence driven by the cooler surface temperatures over the wetlands relative to the adjacent drier surface during the day. The planetary boundary level height (low-level CIN) over the wetlands is higher (lower) than over the large lake during the day, similar to that in Small-Lake.

This study demonstrates that Lake Chad is not acting as a major regional moisture source for convection. Instead, the convective-permitting model results indicate that the regional influence of Lake Chad and its associated wetlands operates through influence on the surface temperature distribution and the atmosphere's dynamical response. Afternoon convection is suppressed over the wetlands and, more strongly, over the large lake due to the differential warming of water and land. This land surface-rainfall relationship is consistent with observations by Taylor et al. (2018), and can be misrepresented in models using cumulus parameterization.

Additionally, our results suggest that the size of the lake/wetland area near Lake Chad influences the local and regional climate. The radius of influence of the daytime lake/wetland

circulation is more spatially confined for a smaller lake compared to a larger lake (Fig. 12), meaning that the areal extent of the subsidence that helps suppress convective activity is more limited.

It is not clear how the size of Lake Chad will change in the future, as the Sahel rainfall recovery associated with greenhouse-gas forcing competes with impacts of agricultural activities and increased surface evaporation due to warmer temperatures. Our study indicates that if the lake and wetlands continue to shrink and/or are lost in the future, afternoon convective activity will increase over the basin of Lake Chad. However, the potential for this negative feedback to maintain or restore the lake is limited.

This study bears the following caveats. The first is that the Wetland experiment misses the afternoon rainfall peak over the wetland area. Future work is needed to evaluate whether this deficiency is associated with the choice of the model physical parameterizations used and/or not running enough ensemble members for each experiment. Another caveat is that the lake surface temperature is prescribed based on limited in-situ observations and is not interactively coupled to the atmosphere. This may be why our simulations do not produce a robust nighttime land breeze in the vicinity of the lake, as our prescribed lake temperatures may not be diurnally realistic. The next step is to evaluate the lake/atmosphere interactions for the Lake Chad region using a coupled CP model.

Acknowledgements

Support from NSF Award #1929074 is gratefully acknowledged. The HPC and database resources needed for the analysis were supplied by the Texas Advanced Computing Center (TACC) at The University of Texas at Austin. URL: http://www.tacc.utexas.edu.

686 References 687 Ashouri H, Hsu K-L, Sorooshian S, et al (2015) PERSIANN-CDR: Daily Precipitation Climate 688 Data Record from Multisatellite Observations for Hydrological and Climate Studies. Bull 689 Am Meteorol Soc 96:69–83. https://doi.org/10.1175/BAMS-D-13-00068.1 690 Bakas NA, Fotiadi A, Kariofillidi S (2020) Climatology of the Boundary Layer Height and of the 691 Wind Field over Greece. Atmosphere (Basel). 11 692 Batjes NH, Ribeiro E, van Oostrum A, et al (2017) WoSIS: providing standardised soil profile 693 data for the world. Earth Syst Sci Data 9:1–14. https://doi.org/10.5194/essd-9-1-2017 694 Biasutti M (2019) Rainfall trends in the African Sahel: Characteristics, processes, and causes. 695 Wiley Interdiscip Rev Clim Chang 10:1–22. https://doi.org/10.1002/wcc.591 696 Birkett CM (2000) Synergistic Remote Sensing of Lake Chad: Variability of Basin Inundation. 697 Remote Sens Environ 72:218–236. https://doi.org/https://doi.org/10.1016/S0034-698 4257(99)00105-4 Bouchez C, Goncalves J, Deschamps P, et al (2016) Hydrological, chemical, and isotopic 699 700 budgets of Lake Chad: a quantitative assessment of evaporation, transpiration and 701 infiltration fluxes. Hydrol Earth Syst Sci 20:1599–1619. https://doi.org/10.5194/hess-20-

Collection 2. Remote Sens 12:. https://doi.org/10.3390/rs12061044
 Buma WG, Lee S II, Seo JY (2018) Recent surface water extent of lake Chad from multispectral
 sensors and GRACE. Sensors (Switzerland) 18:. https://doi.org/10.3390/s18072082
 Carmouze J-P, Lemoalle J (1983) The lacustrine environment. In: Carmouze J-P, Durand J-R,

Lévêque C (eds) Lake Chad: Ecology and Productivity of a Shallow Tropical Ecosystem.

Buchhorn M, Lesiv M, Tsendbazar N-E, et al (2020) Copernicus Global Land Cover Layers—

702

703

708

1599-2016

709 Springer Netherlands, Dordrecht, pp 27–63 710 Chen F, Dudhia J (2001) Coupling and advanced land surface-hydrology model with the Penn 711 State-NCAR MM5 modeling system. Part I: Model implementation and sensitivity. Mon 712 Weather Rev 129:569–585. https://doi.org/10.1175/1520-713 0493(2001)129<0569:CAALSH>2.0.CO;2 714 Cheng WYY, Cotton WR (2004) Sensitivity of a cloud-resolving simulation of the genesis of a 715 mesoscale convective system to horizontal heterogeneities in soil moisture initialization. J 716 Hydrometeorol 5:934–958. https://doi.org/10.1175/1525-717 7541(2004)005<0934:SOACSO>2.0.CO;2 718 Clark DB, Taylor CM, Thorpe AJ (2004) Feedback between the land surface and rainfall at 719 convective length scales. J Hydrometeorol 5:625–639. https://doi.org/10.1175/1525-720 7541(2004)005<0625:FBTLSA>2.0.CO;2 721 Coe MT, Foley JA (2001) Human and natural impacts on the water resources of the Lake Chad 722 basin. J Geophys Res Atmos 106:3349–3356. https://doi.org/10.1029/2000JD900587 723 Cook KH, Vizy EK (2019) Contemporary Climate Change of the African Monsoon Systems. 724 Curr Clim Chang Reports 5:145–159. https://doi.org/10.1007/s40641-019-00130-1 725 Copernicus Climate Change Service (C3S) (2017): ERA5: Fifth generation of ECMWF 726 atmospheric reanalyses of the global climate. Copernicus Climate Change Service Climate 727 Data Store (CDS). https://cds.climate.copernicus.eu/cdsapp#!/home Copernicus Service information [2022]. 728 729 Crétat J, Vizy EK, Cook KH (2015) The relationship between African easterly waves and daily 730 rainfall over West Africa: observations and regional climate simulations. Clim Dyn 44:385– 731 404. https://doi.org/10.1007/s00382-014-2120-x

- 732 Crétaux JF, Birkett C (2006) Lake studies from satellite radar altimetry. Comptes Rendus -
- 733 Geosci 338:1098–1112. https://doi.org/10.1016/j.crte.2006.08.002
- 734 Diallo I, Giorgi F, Stordal F (2018) Influence of Lake Malawi on regional climate from a double-
- nested regional climate model experiment. Clim Dyn 50:3397–3411.
- 736 https://doi.org/10.1007/s00382-017-3811-x
- 737 Donlon CJ, Martin M, Stark J, et al (2012) The Operational Sea Surface Temperature and Sea
- 738 Ice Analysis (OSTIA) system. Remote Sens Environ 116:140–158.
- 739 https://doi.org/https://doi.org/10.1016/j.rse.2010.10.017
- 740 Dudhia J (1989) Numerical Study of Convection Observed during the Winter Monsoon
- Experiment Using a Mesoscale Two-Dimensional Model. J Atmos Sci 46:3077–3107.
- 742 https://doi.org/10.1175/1520-0469(1989)046<3077:NSOCOD>2.0.CO;2
- Duguay–Tetzlaff A, Stöckli R, Bojanowski J, Hollmann R, Fuchs P, Werscheck M (2017) CM
- SAF Land SUrface Temperature dataset from METeosat First and Second Generation -
- Edition 1 (SUMET Ed. 1). Satellite Application Facility on Climate Monitoring.
- 746 DOI:10.5676/EUM SAF CM/LST METEOSAT/V001.
- 747 https://doi.org/10.5676/EUM SAF CM/LST METEOSAT/V001
- 748 Ek MB, Holtslag AAM (2004) Influence of soil moisture on boundary layer cloud development.
- 749 J Hydrometeorol 5:86–99. https://doi.org/10.1175/1525-
- 750 7541(2004)005<0086:IOSMOB>2.0.CO;2
- 751 Emori S (1998) The interaction of cumulus convection with soil moisture distribution: An
- 752 idealized simulation. J Geophys Res 103:8873–8884
- 753 Fairall CW, Bradley EF, Hare JE, et al (2003) Bulk parameterization of air-sea fluxes: Updates
- and verification for the COARE algorithm. J Clim 16:571–591.

755	https://doi.org/10.1175/1520-0442(2003)016<0571:BPOASF>2.0.CO;2
756	Findell KL, Eltahir EAB (2003a) Atmospheric controls on soil moisture-boundary layer
757	interactions. Part II: Feedbacks within the continental United States. J Hydrometeorol
758	4:570–583. https://doi.org/10.1175/1525-7541(2003)004<0570:ACOSML>2.0.CO;2
759	Findell KL, Eltahir EAB (2003b) Atmospheric controls on soil moisture-boundary layer
760	interactions. Part I: Framework development. J Hydrometeorol 4:552-569.
761	https://doi.org/10.1175/1525-7541(2003)004<0552:ACOSML>2.0.CO;2
762	Finney DL, Marsham JH, Jackson LS, et al (2019) Implications of improved representation of
763	convection for the East Africa water budget using a convection-permitting model. J Clim
764	32:2109–2129. https://doi.org/10.1175/JCLI-D-18-0387.1
765	Funk C, Peterson P, Landsfeld M, et al (2015) The climate hazards infrared precipitation with
766	stationsa new environmental record for monitoring extremes. Sci data 2:150066.
767	https://doi.org/10.1038/sdata.2015.66
768	Funk CC, Peterson PJ, Landsfeld MF, et al (2014) A quasi-global precipitation time series for
769	drought monitoring. Reston, VA
770	Gao H, Bohn TJ, Podest E, et al (2011) On the causes of the shrinking of Lake Chad. Environ
771	Res Lett 6:. https://doi.org/10.1088/1748-9326/6/3/034021
772	Hohenegger C, Brockhaus P, Bretherton CS, Schär C (2009) The soil moisture-precipitation
773	feedback in simulations with explicit and parameterized convection. J Clim 22:5003-5020
774	https://doi.org/10.1175/2009JCLI2604.1
775	Hong SY, Noh Y, Dudhia J (2006) A new vertical diffusion package with an explicit treatment
776	of entrainment processes. Mon Weather Rev 134:2318–2341.
777	https://doi.org/10.1175/MWR3199.1

778 Huffman GJ, Bolvin DT, Nelkin EJ, et al (2007) The TRMM Multisatellite Precipitation 779 Analysis (TMPA): Quasi-Global, Multiyear, Combined-Sensor Precipitation Estimates at 780 Fine Scales. J Hydrometeorol 8:38–55. https://doi.org/10.1175/JHM560.1 781 Huffman GJ, Stocker EF, Bolvin DT, Nelkin EJ, Tan J (2019) GPM IMERG Final Precipitation 782 L3 Half Hourly 0.1 degree x 0.1 degree V06, Greenbelt, MD, Goddard Earth Sciences Data 783 and Information Services Center (GES DISC). 10.5067/GPM/IMERG/3B-HH/06 784 Hutchinson TA (2009) An Adaptive Time-Step for Increased Model Efficiency. Ext Abstr 785 Eighth WRF Users' Work 4 786 Janicot S, Kamga F (2015) Key research and prediction challenges for West and Central Africa. 787 CLIVAR Exch (no 66) 19:10–15 Jeworrek J, West G, Stull R (2019) Evaluation of cumulus and microphysics parameterizations 788 789 in WRF across the convective gray zone. Weather Forecast 34:1097–1115. 790 https://doi.org/10.1175/WAF-D-18-0178.1 791 Jiménez-Esteve B (2016) Land use influence in WRF model. A high resolution mesoscale 792 modeling over Oriental Pyrenees. 793 Jiménez PA, Dudhia J, González-Rouco JF, et al (2012) A Revised Scheme for the WRF Surface 794 Layer Formulation. Mon Weather Rev 140:898–918. https://doi.org/10.1175/MWR-D-11-795 00056.1 796 Joyce RJ, Janowiak JE, Arkin PA, Xie P (2004) CMORPH: A Method that Produces Global 797 Precipitation Estimates from Passive Microwave and Infrared Data at High Spatial and Temporal Resolution. J Hydrometeorol 5:487–503. https://doi.org/10.1175/1525-798 799 7541(2004)005<0487:CAMTPG>2.0.CO;2 800 Kain JS (2004) The Kain-Fritsch Convective Parameterization: An Update. J Appl Meteorol

801	43:170–181. https://doi.org/10.1175/1520-0450(2004)043<0170:TKCPAU>2.0.CO;2
802	Kendon EJ, Roberts NM, Senior CA, Roberts MJ (2012) Realism of rainfall in a very high-
803	resolution regional climate model. J Clim 25:5791–5806. https://doi.org/10.1175/JCLI-D-
804	11-00562.1
805	Koseki S, Mooney PA (2019) Influences of Lake Malawi on the spatial and diurnal variability of
806	local precipitation. Hydrol Earth Syst Sci 23:2792–2812. https://doi.org/10.5194/hess-23-
807	2795-2019
808	Laing AG, Trier SB, Davis CA (2012) Numerical simulation of episodes of organized
809	convection in tropical Northern Africa. Mon Weather Rev 140:2874-2886.
810	https://doi.org/10.1175/MWR-D-11-00330.1
811	Lauwaet D, van Lipzig NPM, Van Weverberg K, et al (2012) The precipitation response to the
812	desiccation of Lake Chad. Q J R Meteorol Soc 138:707-719. https://doi.org/10.1002/qj.942
813	Leblanc M, Leduc C, Razack M, et al (2003) Applications of remote sensing and GIS for
814	groundwater modelling of large semiarid areas: Example of the Lake Chad Basin, Africa.
815	IAHS-AISH Publ 186–194
816	Leblanc M, Lemoalle J, Bader JC, et al (2011) Thermal remote sensing of water under flooded
817	vegetation: New observations of inundation patterns for the "Small" Lake Chad. J Hydrol
818	404:87–98. https://doi.org/10.1016/j.jhydrol.2011.04.023
819	Lemoalle J (2005) The Lake Chad basin. In: Fraser LH, Keddy PA (eds) The World's Largest
820	Wetlands: Ecology and Conservation. pp 316–346
821	Lemoalle J (2004) Lake Chad: A Changing Environment. 321–339. https://doi.org/10.1007/978-
822	94-007-0967-6_13
823	Lemoalle J, Bader JC, Leblanc M, Sedick A (2012) Recent changes in Lake Chad: Observations

824	simulations and management options (1973-2011). Glob Planet Change 80-81:247-254.
825	https://doi.org/10.1016/j.gloplacha.2011.07.004
826	Lenters JD, Cook KH (1995) Simulation and Diagnosis of the Regional Summertime
827	Precipitation Climatology of South America. J Clim 8:2988–3005
828	Li J, Han Y, Liu W, et al (2022) A new theoretical model deriving planetary boundary layer
829	height in desert regions and its application on dust devil emissions. Sci Total Environ
830	814:152378. https://doi.org/10.1016/j.scitotenv.2021.152378
831	Li Z, Lyu S, Wen L, et al (2018) Effect of roughness lengths on surface energy and the planetary
832	boundary layer height over high-altitude Ngoring Lake. Theor Appl Climatol 133:1191-
833	1205. https://doi.org/10.1007/s00704-017-2258-7
834	López-Espinoza E, Ruiz-Angulo A, Zavala-Hidalgo J, et al (2019) Impacts of the desiccated lake
835	system on precipitation in the basin of Mexico City. Atmosphere (Basel) 10:1-18.
836	https://doi.org/10.3390/atmos10100628
837	Merchant CJ and MacCallum SN (2018) Lake Surface Water Temperature ARC-Lake v3 (1995-
838	2012). University of Reading. Dataset. http://dx.doi.org/10.17864/1947.186
839	Mlawer EJ, Taubman SJ, Brown PD, et al (1997) Radiative transfer for inhomogeneous
840	atmospheres: RRTM, a validated correlated-k model for the longwave. J Geophys Res
841	Atmos 102:16663-16682. https://doi.org/https://doi.org/10.1029/97JD00237
842	Mohamed YA, Savenije HHG, Bastiaanssen WGM, Van Den Hurk BJJM (2006) New lessons on
843	the Sudd hydrology learned from remote sensing and climate modeling. Hydrol Earth Syst
844	Sci 10:507-518. https://doi.org/10.5194/hess-10-507-2006
845	Mohamed YA, Van Den Hurk BJJM, Savenije HHG, Bastiaanssen WGM (2005) Impact of the
846	Sudd wetland on the Nile hydroclimatology. Water Resour Res 41:1–14.

847	https://doi.org/10.1029/2004WR003792
848	Negri AJ, Adler RF, Xu L, Surratt J (2004) The Impact of Amazonian Deforestation on Dry
849	Season Rainfall. J Clim 17:1306–1319. https://doi.org/10.1175/1520-
850	0442(2004)017<1306:TIOADO>2.0.CO;2
851	Ngounou BN (2009) Water Resources Protection in the Lake Chad Basin in the Changing
852	Environment. Eur Water 25:3–12
853	Nicholson SE, Fink AH, Funk C (2018) Assessing recovery and change in West Africa's rainfall
854	regime from a 161-year record. Int J Climatol 38:3770–3786.
855	https://doi.org/10.1002/joc.5530
856	Novella NS, Thiaw WM (2013) African rainfall climatology version 2 for famine early warning
857	systems. J Appl Meteorol Climatol 52:588-606. https://doi.org/10.1175/JAMC-D-11-
858	0238.1
859	Odada EO, Oyebande L, Oguntola AJ (2005) Lake Chad: experience and lessons learned brief.
860	Kusatsu, Japan
861	Okpara UT, Stringer LC, Dougill AJ (2016) Lake drying and livelihood dynamics in Lake Chad:
862	Unravelling the mechanisms, contexts and responses. Ambio 45:781–795.
863	https://doi.org/10.1007/s13280-016-0805-6
864	Onamuti OY, Okogbue EC, Orimoloye IR (2017) Remote sensing appraisal of Lake Chad
865	shrinkage connotes severe impacts on green economics and socio-economics of the
866	catchment area. R Soc Open Sci 4:171120. https://doi.org/10.1098/rsos.171120
867	Onuoha F (2009) Environmental Degradation, Livelihood and Conflicts: A Focus on the
868	Implications of the Diminishing Water Resources of Lake Chad for North-Eastern Nigeria.
869	African J Confl Resolut 8:35-61. https://doi.org/10.4314/ajcr.v8i2.39425

870	Pham-Duc B, Sylvestre F, Papa F, et al (2020) The Lake Chad hydrology under current climate
871	change. Sci Rep 10:1-10. https://doi.org/10.1038/s41598-020-62417-w
872	Prein AF, Langhans W, Fosser G, et al (2015) A review on regional convection-permitting
873	climate modeling: Demonstrations, prospects, and challenges. Rev Geophys 53:323–361.
874	https://doi.org/10.1002/2014RG000475
875	Prigent C, Rochetin N, Aires F, et al (2011) Impact of the inundation occurrence on the deep
876	convection at continental scale from satellite observations and modeling experiments. J
877	Geophys Res Atmos 116:. https://doi.org/10.1029/2011JD016311
878	Rabin RM, Stadler S, Wetzel PJ, et al (1990) Observed effects of landscape variability on
879	convective clouds. Bull - Am Meteorol Soc 71:272–280. https://doi.org/10.1175/1520-
880	0477(1990)071<0272:OEOLVO>2.0.CO;2
881	Samuelsson P, Tjernström M (2001) Mesoscale flow modification induced by land-lake surface
882	temperature and roughness differences. J Geophys Res Atmos 106:12419–12435.
883	https://doi.org/10.1029/2001JD900057
884	Sarch MT, Birkett C (2000) Fishing and farming at Lake Chad: Responses to lake-level
885	fluctuations. Geogr J 166:156–172. https://doi.org/10.1111/j.1475-4959.2000.tb00015.x
886	Seager R, Henderson N (2013) Diagnostic computation of moisture budgets in the ERA-interim
887	reanalysis with reference to analysis of CMIP-archived atmospheric model data. J Clim
888	26:7876-7901. https://doi.org/10.1175/JCLI-D-13-00018.1
889	Segal M, Garratt JR, Pielke RA, et al (1989) The Impact of Crop Areas in Northeast Colorado or
890	Midsummer Mesoscale Thermal Circulations. Mon Weather Rev 117:809–825.
891	https://doi.org/10.1175/1520-0493(1989)117<0809:TIOCAI>2.0.CO;2
892	Segal M, Pan Z, Turner RW, Takle ES (1998) On the potential impact of irrigated areas in North

893	America on summer rainfall caused by large-scale systems. J Appl Meteorol 37:325–331.
894	https://doi.org/10.1175/1520-0450-37.3.325
895	Skamarock WC, Klemp JB, Dudhia J, Gill DO, Liu Z, Berner J, Huang X-yu (2019) A
896	Description of the Advanced Research WRF Model Version 4.1 (No. NCAR/TN-
897	556+STR). doi:10.5065/1dfh-6p97
898	Soboyejo LA, Sakinat AM, Bankole AO (2021) A DPSIR and SAF Analysis of Water Insecurity
899	in Lake Chad Basin, Central Africa. Proc Int Assoc Hydrol Sci 384:313-318.
900	https://doi.org/10.5194/piahs-384-313-2021
901	Stull R (2006) The Atmospheric Boundary Layer. In: Wallace JM, Hobbs PV (eds) Atmospheric
902	Science (Second Edition). Academic Press, pp 375-417
903	Tappan GG, Cushing WM, Cotillon SE, et al (2016) West Africa Land Use Land Cover Time
904	Series: U.S. Geological Survey data release. https://doi.org/10.5066/F73N21JF
905	Tarnavsky E, Grimes D, Maidment R, et al (2014) Extension of the TAMSAT Satellite-Based
906	Rainfall Monitoring over Africa and from 1983 to Present. J Appl Meteorol Climatol
907	53:2805–2822. https://doi.org/10.1175/JAMC-D-14-0016.1
908	Taylor CM (2010) Feedbacks on convection from an African wetland. Geophys Res Lett 37:1–7.
909	https://doi.org/10.1029/2009GL041652
910	Taylor CM, Birch CE, Parker DJ, et al (2013) Modeling soil moisture-precipitation feedback in
911	the Sahel: Importance of spatial scale versus convective parameterization. Geophys Res Let
912	40:6213-6218. https://doi.org/10.1002/2013GL058511
913	Taylor CM, De Jeu RAM, Guichard F, et al (2012) Afternoon rain more likely over drier soils.
914	Nature 489:423-426. https://doi.org/10.1038/nature11377
915	Taylor CM, Ellis RJ (2006) Satellite detection of soil moisture impacts on convection at the

916	mesoscale. Geophys Res Lett 33:11–14. https://doi.org/10.1029/2005GL025252
917	Taylor CM, Klein C, Parker DJ, et al (2022) "Late-stage" deforestation enhances storm trends in
918	coastal West Africa. Proc Natl Acad Sci 119:e2109285119.
919	https://doi.org/10.1073/pnas.2109285119
920	Taylor CM, Lebel T (1998) Observational evidence of persistent convective-scale rainfall
921	patterns. Mon Weather Rev 126:1597-1607. https://doi.org/10.1175/1520-
922	0493(1998)126<1597:OEOPCS>2.0.CO;2
923	Taylor CM, Prigent C, Dadson SJ (2018) Mesoscale rainfall patterns observed around wetlands
924	in sub-Saharan Africa. Q J R Meteorol Soc 144:2118–2132. https://doi.org/10.1002/qj.3311
925	Taylor CM, Saïd F, Lebel T (1997) Interactions between the land surface and mesoscale rainfall
926	variability during HAPEX-Sahel. Mon Weather Rev 125:2211-2227.
927	https://doi.org/10.1175/1520-0493(1997)125<2211:IBTLSA>2.0.CO;2
928	Thiery W, Davin EL, Panitz HJ, et al (2015) The impact of the African Great Lakes on the
929	regional climate. J Clim 28:4061-4085. https://doi.org/10.1175/JCLI-D-14-00565.1
930	Thompson G, Field PR, Rasmussen RM, Hall WD (2008) Explicit Forecasts of Winter
931	Precipitation Using an Improved Bulk Microphysics Scheme. Part II: Implementation of a
932	New Snow Parameterization. Mon Weather Rev 136:5095–5115.
933	https://doi.org/10.1175/2008MWR2387.1
934	Tian Y, Peters-Lidard CD (2007) Systematic anomalies over inland water bodies in satellite-
935	based precipitation estimates. Geophys Res Lett 34:
936	https://doi.org/https://doi.org/10.1029/2007GL030787
937	UNEP (2006) Africa's Lakes: Atlas of Our Changing Environment. Division of Early Warning
938	and Assessment (DEWA), United Nations Environment Programme (UNEP), P.O. Box

939	30552 Nairobi, Kenya
940	Vizy EK, Cook KH (2009) Tropical storm development from African easterly waves in the
941	Eastern Atlantic: A comparison of two successive waves using a regional model as part of
942	NASA AMMA 2006. J Atmos Sci 66:3313–3334. https://doi.org/10.1175/2009JAS3064.1
943	Vizy EK, Cook KH (2018) Mesoscale convective systems and nocturnal rainfall over the West
944	African Sahel: role of the Inter-tropical front. Clim Dyn 50:587-614.
945	https://doi.org/10.1007/s00382-017-3628-7
946	Vizy EK, Cook KH (2019) Understanding the summertime diurnal cycle of precipitation over
947	sub-Saharan West Africa: regions with daytime rainfall peaks in the absence of significant
948	topographic features. Clim Dyn 52:2903–2922. https://doi.org/10.1007/s00382-018-4315-z
949	Vizy EK, Cook KH, Crétat J, Neupane N (2013) Projections of a wetter sahel in the twenty-first
950	century from global and regional models. J Clim 26:4664-4687.
951	https://doi.org/10.1175/JCLI-D-12-00533.1
952	Wan Z, Hook S, Hulley G (2015) MOD11C1 MODIS/Terra Land Surface
953	Temperature/Emissivity Daily L3 Global 0.05Deg CMG V006. NASA EOSDIS Land
954	Processes DAAC. https://doi.org/10.5067/MODIS/MOD11C1.006
955	Woodhams BJ, Birch CE, Marsham JH, et al (2019) Identifying key controls on storm formation
956	over the lake Victoria basin. Mon Weather Rev 147:3365–3390.
957	https://doi.org/10.1175/MWR-D-19-0069.1
958	Yunana DA, Shittu AA, Ayuba S, et al (2017) Climate change and lake water resources in Sub-
959	Saharan Africa: case study of lake Chad and lake Victoria. Niger J Technol 36:648.
960	https://doi.org/10.4314/njt.v36i2.42
961	Zhang Y, Gao Z, Li D, et al (2014) On the computation of planetary boundary-layer height using

962	the bulk Richardson number method. Geosci Model Dev 7:2599–2611.
963	https://doi.org/10.5194/gmd-7-2599-2014
964	Zhu W, Jia S, Lall U, et al (2019) Relative contribution of climate variability and human
965	activities on the water loss of the Chari/Logone River discharge into Lake Chad: A
966	conceptual and statistical approach. J Hydrol 569:519-531.
967	https://doi.org/10.1016/j.jhydrol.2018.12.015
968	Zhu W, Yan J, Jia S (2017) Monitoring recent fluctuations of the southern pool of lake chad
969	using multiple remote sensing data: Implications for water balance analysis. Remote Sens
970	9:. https://doi.org/10.3390/rs9101032
971	
972	Statements and Declarations:
973	Funding: This work was funded by NSF Award #1929074
974	Conflict of interest: Not applicable
975	Availability of data: All datasets analyzed in this study are freely available from their original
976	sources. Model data available from author on request
977	Code availability: Not applicable

Table 1 Specifications for the four experiments

	Land Use Specifications for the		Ensemble
Experiments	3-km Domain	Representation	Members
Small-Lake	 A small Lake Chad of 1314 km². (The lake area is 729 km² and 1296 km² in the 27-km and 9-km domains, respectively.) Adjacent herbaceous wetlands of 23607 km², with soil saturation decreasing from ~39% to 30% (~0.18 to 0.14 m³/m³) and from 28% to 24% (0.13 to 0.11 m³/m³) and being roughly constant at 40% and 41% (~0.19 m³/m³) in the 0-10 cm, 10-40 cm, 40-100 cm and 100-200 cm soil layers through August, respectively. Vegetation fraction (output from greenness fraction) over the wetlands increases from 28.99 to 50.39, and decreases to 50.09 through August. 	Lake Chad of 1314 the lake area is 729 km² 6 km² in the 27-km and omains, respectively.) In therbaceous wetlands 7 km², with soil on decreasing from o 30% (~0.18 to 0.14 and from 28% to 24% o 0.11 m³/m³) and being o constant at 40% and o 0.19 m³/m³) in the 0-10 40 cm, 40-100 cm and o cm soil layers through o respectively. cion fraction (output eenness fraction) over lands increases from o 50.39, and decreases	
Large-Lake	A large Lake Chad of 24921 km ² .	1960's climate, or contemporary years with anomalously large river input.	5
Wetland	A small Lake Chad of 1314 km² (with adjusted lake surface temperatures; Fig. 2). Adjacent herbaceous wetlands of 24138 km², with soil moisture maintained at 58% saturated (0.2697 m³/m³) and vegetation fraction constant at 44.7 through August.		3
Large-Lake-II	A large Lake Chad of 25452 km ² (with adjusted lake surface temperatures; Fig. 2).	The comparative experiment to Wetland, and a sensitivity test to Large-Lake.	3

Table 2 Datasets for lake temperatures over Lake Chad

Dataset	Long Name	Spatial Resolution	Temporal Resolution	Analysis Period
SUMET	The CM SAF Land SUrface Temperature dataset from METeosat First and Second Generation - Edition 1 (Duguay–Tetzlaff et al. 2017)	0.05°	Monthly- diurnal	1991 – 2015
ERA5	The ERA5 lake mixed-layer temperatures (Copernicus Climate Change Service 2017)	0.25°	Hourly	1979 – 2019
MOD11C1	The MODIS/Terra Land Surface Temperature/Emissivity L3 Global CMG Version 6 (Wan et al. 2015)	0.05°	Daily	2001 – 2019
ARC-Lake	The Merged-ATSR observations from the ATSR Reprocessing for Climate: Lake Surface Water Temperature & Ice Cover v3 (Merchant and MacCallum 2018)	0.05°	Twice- monthly	1995 – 2012
ILEC	The International Lake Environment Committee database (wldb.ilec.or.jp)	NA	NA	NA*

^{*} The analysis period for the temperature range of 299 – 309 K in ILEC data is 1956-1960. The temperature value of 297 K (converted from 24.2 °C) in IELC data is for Bol Dune, and the analysis period is not available.

Table 3 Precipitation datasets used to evaluate the model simulations

able 3 Precipitation datasets used to evaluate the model simulations				
Dataset	Long Name	Spatial Resolution	Temporal Resolution	
IMERG	The final run product of the NASA Integrated Multi-satellitE Retrievals for GPM L3 V06 (Huffman et al. 2019)	0.1°	30-min	
СМОРРН	The Climate Prediction Center morphing technique precipitation dataset version 1.0 (Joyce et al. 2004)	8-km	30-min	
CHIRPS2	The Climate Hazards Group InfraRed Precipitation with Station data version 2.0 (Funk et al. 2014)	0.05°	Daily	
TARCAT	The Tropical Applications of Meteorology using SATellite and ground-based observations (TAMSAT) African Rainfall Climatology And Time series (Tarnavsky et al. 2014)	0.0375°	Daily	
ARC2	The Climate Prediction Center Africa Rainfall Climatology version 2.0 (Novella and Thiaw 2013)	0.1°	Daily	
PERSIANN- CDR	The Precipitation Estimation from Remotely Sensed Information using Artificial Neural Networks- Climate Data Record (Ashouri et al. 2015)	0.25°	Daily	
TMPA	Tropical Rainfall Measurement Mission Multi-satellite Precipitation Analysis (Huffman et al. 2007)	0.25°	3-hourly	

Figure Captions

Fig.1 a Terrain height (m; shading) and model configuration for the triple-nested domains. **b-e** Land use types prescribed in the 3-km domain of Small-Lake, Large-Lake, Wetland and Large-Lake-II. The averaging region for the wetland area (including the area at 13.5°N and 13.9°E) is

stippled. The locations of rivers that flow into Lake Chad are drawn by hand in Fig. 1b

averaging region for SUMET

Fig.2 a August mean temperatures (K) over Lake Chad from SUMET, ERA5, MOD11C1, ARC-Lake and IELC, averaged over their individual record lengths. Temperatures are averaged over all available data points for ARC-Lake and over interpolated lake masks for the other gridded datasets. b Prescribed temperatures (K) over Lake Chad in the 3-km domain of Small-Lake and Wetland. c Observed and simulated surface temperatures (K) over the wetland area from SUMET, all three domains of Small-Lake and 3-km domain of Wetland. The wetland area as the averaging region for Small-Lake/Wetland is stippled in Fig. 1b and is interpolated to the

Fig.3 August mean precipitation (mm·day⁻¹) averaged over 2000 – 2019 from **a** IMERG, **b** CMORPH and **c** CHIRPS2. Ensemble mean precipitation from the **d** 27-km, **e** 9-km and **f** 3-km domains of Small-Lake simulations. The latitudinal and longitudinal ranges are from the 3-km domain.

Fig.4 a 875-hPa and **b** 600-hPa specific humidity (10⁻³ kg·kg⁻¹; shading), geopotential (m²·s⁻²; contours) and horizontal wind (m·s⁻¹; vectors) in August from ERA5, averaged over 1979-2019.

The contours and vectors are plotted every 6 grids for clarity. **c** 875-hPa and **d** 600-hPa specific humidity, geopotential and horizontal wind in August from the ensemble mean of Small-Lake in the 3-km domain. The contours and vectors are plotted every 50 grids for clarity

Fig.5 August mean rainfall (mm·day⁻¹) from **a** IMERG, **b** CMORPH, **c** CHIRPS2, **d** TARCAT, **e** ARC2 and **f** PERSIANN for 2000-2019. Ensemble mean rainfall from the 3-km domains of **g** Small-Lake and **h** Wetland. Black triangles denote the locations of in-situ data incorporated in CHIRPS2

Fig.6 Precipitation (mm·day⁻¹) diurnal cycle area-averaged over Lake Chad in **a** observations, **b** Small-lake and **c** Wetland during August. Precipitation diurnal cycle over the wetlands in **d** observations, **e** Small-lake and **f** Wetland during August. The wetland area as the averaging region is stippled in Fig. 1b. The averaging regions for IMERG, CMORPH and TMPA are interpolated from the lake/wetland area in the 9-km, 9-km and 27-km domains of Small-Lake, respectively

Fig.7 a Rainfall difference (mm·day⁻¹) between the Large-Lake and Small-Lake ensemble means in the 3-km domain. Values at or exceeding the 95% confidence level based on a Welch's t-test are stippled. **b** Diurnal cycle of precipitation (mm·day⁻¹) averaged over the wetland area (stippled in Fig.1b) from the Small-Lake, Large-Lake, and Large-Lake-II ensemble means. Dots denote differences between Small-Lake and the two large-lake experiments that exceed the 95% confidence level based on Welch's t-tests

Fig.8 Anomalies of MSE and its terms (10³ J·kg⁻¹), differenced between Large-Lake and Small-Lake at a 15Z and b 00Z for the dry-hour composite averaged over the wetland area. Diurnal cycle of 950-hPa CIN (J·kg⁻¹) in Small-Lake and Large-Lake-I for the c dry- and d rainy-day composites. Dots denote values exceeding the 95% confidence level based on Welch's t-tests Fig.9 Diurnal cycle of specific humidity (kg·kg⁻¹) over the wetland area in a Small-Lake and b Large-Lake for the dry days composites. Diurnal cycle of the time rate change of specific humidity (s⁻¹) over the wetland area in c Small-Lake and d Large-Lake. Diurnal cycle of the moisture flux convergence (s⁻¹) over the wetland area in e Small-Lake and f Large-Lake. Diurnal cycle of the residual term (s⁻¹) over the wetland area in **g** Small-Lake and **h** Large-Lake. Dots denote differences between Small-Lake and Large-Lake that exceed the 95% confidence level based on Welch's t-tests Fig.10 Diurnal cycle of water in non-gas (cloud, rain, ice, snow, and graupel) phase (kg·kg⁻¹) over the wetland area in a Small-Lake and b Large-Lake for the dry-day composite. The time and geopotential height (GHT; m) of the daytime maximum relative humidity (%; square) at 925-625 hPa, and the PBLH (m) over the wetland area in a Small-Lake and b Large-Lake for the dry-day composite. Dots denote differences between Small-Lake and Large-Lake that exceed the 95% confidence level based on a Welch's t-test Fig.11 The planetary boundary layer height (PBLH; m; solid line) and the level of free

1036

1037

1038

1039

1040

1041

1042

1043

1044

1045

1046

1047

1048

1049

1050

1051

1052

1053

1054

1055

1056

1057

1058

convection (LFC; m; dashed line) in Small-Lake and Large-Lake over the wetland area, for the **a** dry- and **b** rainy-day composites. **c** Sensible heat flux (SH; W·m⁻²; solid line) and anomalous

potential temperature between 700 hPa and 950 hPa ($\Delta\theta$; K; dashed line) in Small-Lake and Large-Lake over the wetland area, for the dry-day composite. **d** Vertical p-velocity at the pressure level closest to the PBLH (ω ; Pa·s⁻¹) in Small-Lake and Large-Lake over the wetland area, for the dry-day composite. **e** Differences of sensible heat flux (W·m⁻²) between the Large-Lake and Small-Lake ensemble means, for the dry-day composite. **f** Anomalies between the surface and 2 m temperatures (-(T_{2m}-T_g); K; solid line) and the 10-m wind speed (m·s⁻¹; dashed line) in Small-Lake and Large-Lake over the wetland area, for the dry-day composite. Dots denote differences between Small-Lake and Large-Lake that exceed the 95% confidence level based on Welch's t-tests

Fig.12 a 2m-temperature (K; shading) and 10-m horizontal wind (m·s⁻¹) at 12Z in Small-Lake for the dry-day composite. **b** Vertical cross sections of the zonal wind (m·s⁻¹) and vertical p-velocity (Pa·s⁻¹) at 12Z in Small-Lake for the dry-day composite averaged over the latitudes of the small lake. **c-d** are similar to **a-b**, but for Large-Lake. **e-f** are differences between Large-Lake and Small-Lake. The longitudes of the small and the large lake are marked by light and dark blue bars, respectively. Values exceeding the 95% confidence level are shown in shading or denoted by green vectors based on Welch's t-tests. Vectors are plotted every 6 grids in **a**, **c** and **e**, and every 3 grids in longitudes in the vertical cross sections for clarity

Fig.13 Material acceleration of the 875-hPa vertical p-velocity (Pa·s⁻²) at 12Z in **a** Small-Lake and **b** Large-Lake for the dry-day composite. **c** plots the differences between Large-Lake and Small-Lake. Values exceeding the 95% confidence level are shown in shading based on Welch's t-tests.

1082 Fig.14 Daily-mean differences of a Precipitation, b evapotranspiration, c horizontal moisture 1083 convergence and **d** the residual term (mm·day⁻¹; Eqn. 2) between the Large-Lake and Small-Lake 1084 1085 ensemble means. Values at or exceeding the 95% confidence level are stippled based on Welch's 1086 t-tests 1087 Fig.15 a Diurnal cycle of precipitation (mm·day⁻¹) over the wetland area from the Small-Lake, 1088 Large-Lake-II, and Wetland ensemble mean. **b** The PBLH (m) over the wetland area from the 1089 Small-Lake, Large-Lake-II, and Wetland ensemble mean. c Diurnal cycle of 825-hPa vertical p-1090 velocity (Pa·s⁻¹) over the wetland area in Small-Lake, Large-Lake-II, and Wetland for the dry-1091 1092 day composite. Dots denote differences between Small-Lake and the other two experiments that exceed the 95% confidence level based on Welch's t-test. 1093

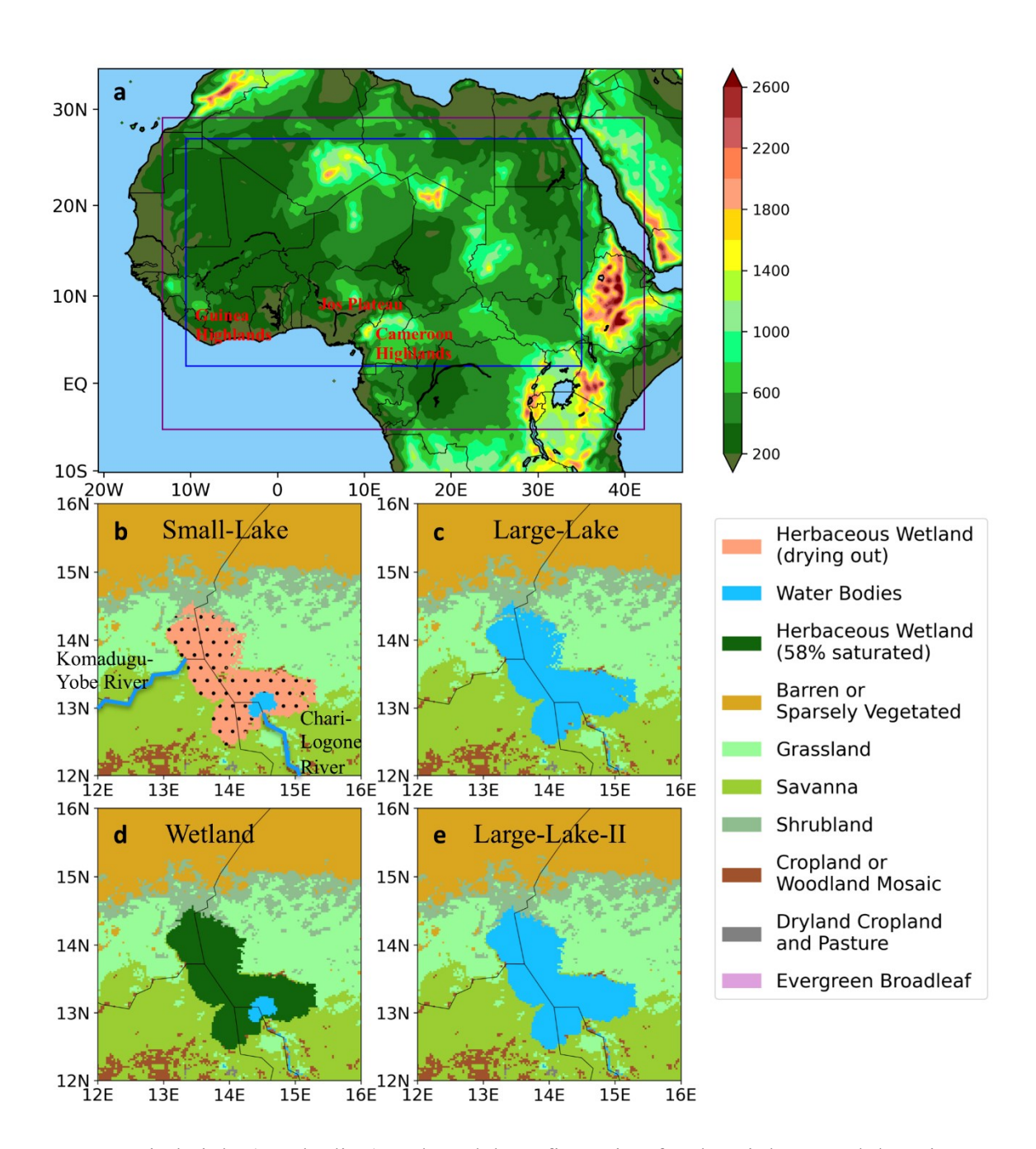


Fig.1 a Terrain height (m; shading) and model configuration for the triple-nested domains. **b-e** Land use types prescribed in the 3-km domain of Small-Lake, Large-Lake, Wetland and Large-Lake-II. The averaging region for the wetland area is stippled. The locations of rivers that flow into Lake Chad are drawn by hand in Fig. 1b

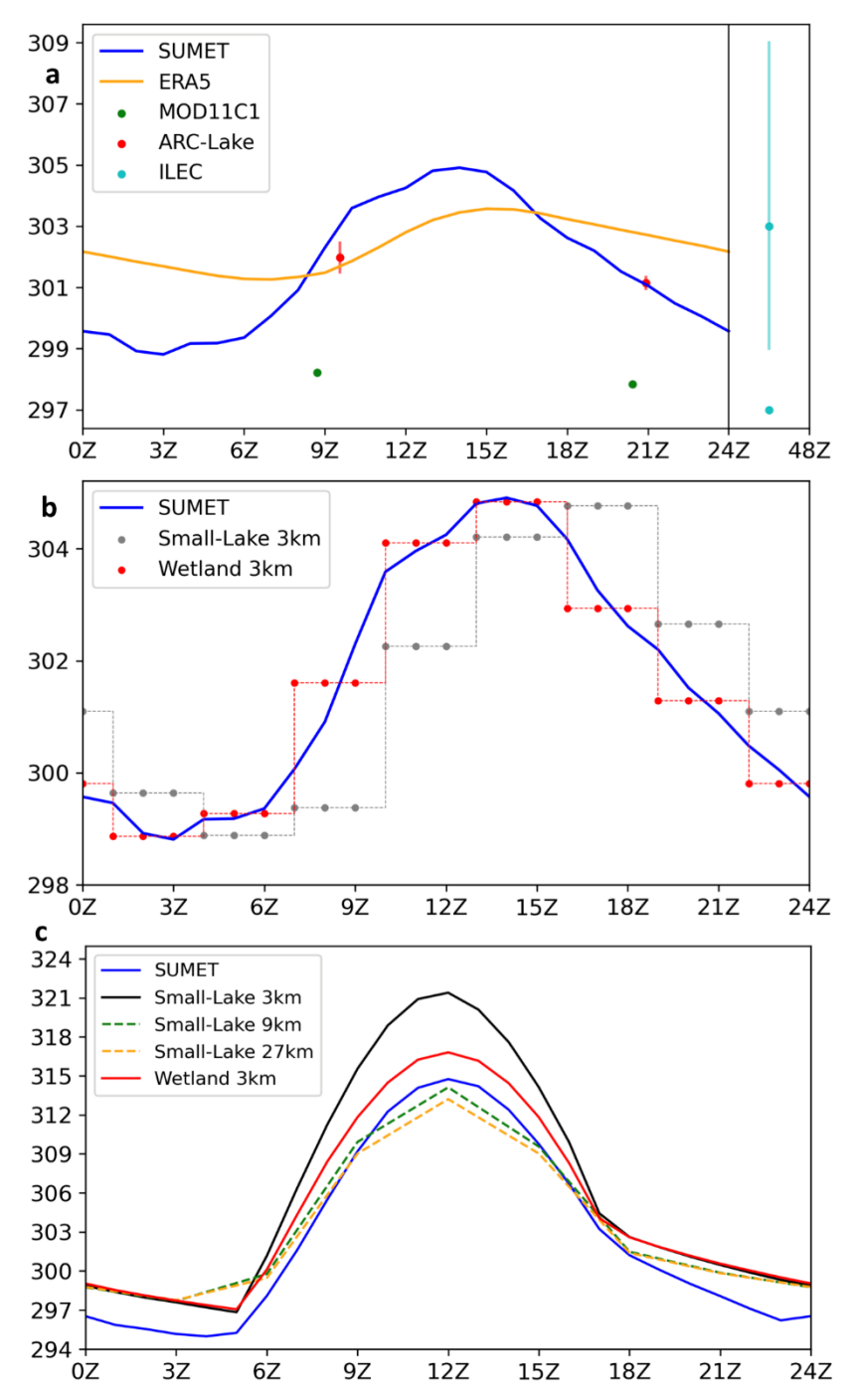


Fig.2 a August mean temperatures (K) over Lake Chad from SUMET, ERA5, MOD11C1, ARC-Lake and IELC, averaged over their individual record lengths. Temperatures are averaged over all available data points for ARC-Lake and over interpolated lake masks for the other gridded datasets. **b** Prescribed temperatures (K) over Lake Chad in the 3-km domain of Small-Lake and Wetland. **c** Observed and simulated surface temperatures (K) over the wetland area from SUMET, all three domains of Small-Lake and 3-km domain of Wetland. The wetland area as the averaging region for Small-Lake/Wetland is stippled in Fig. 1b and is interpolated to the averaging region for SUMET

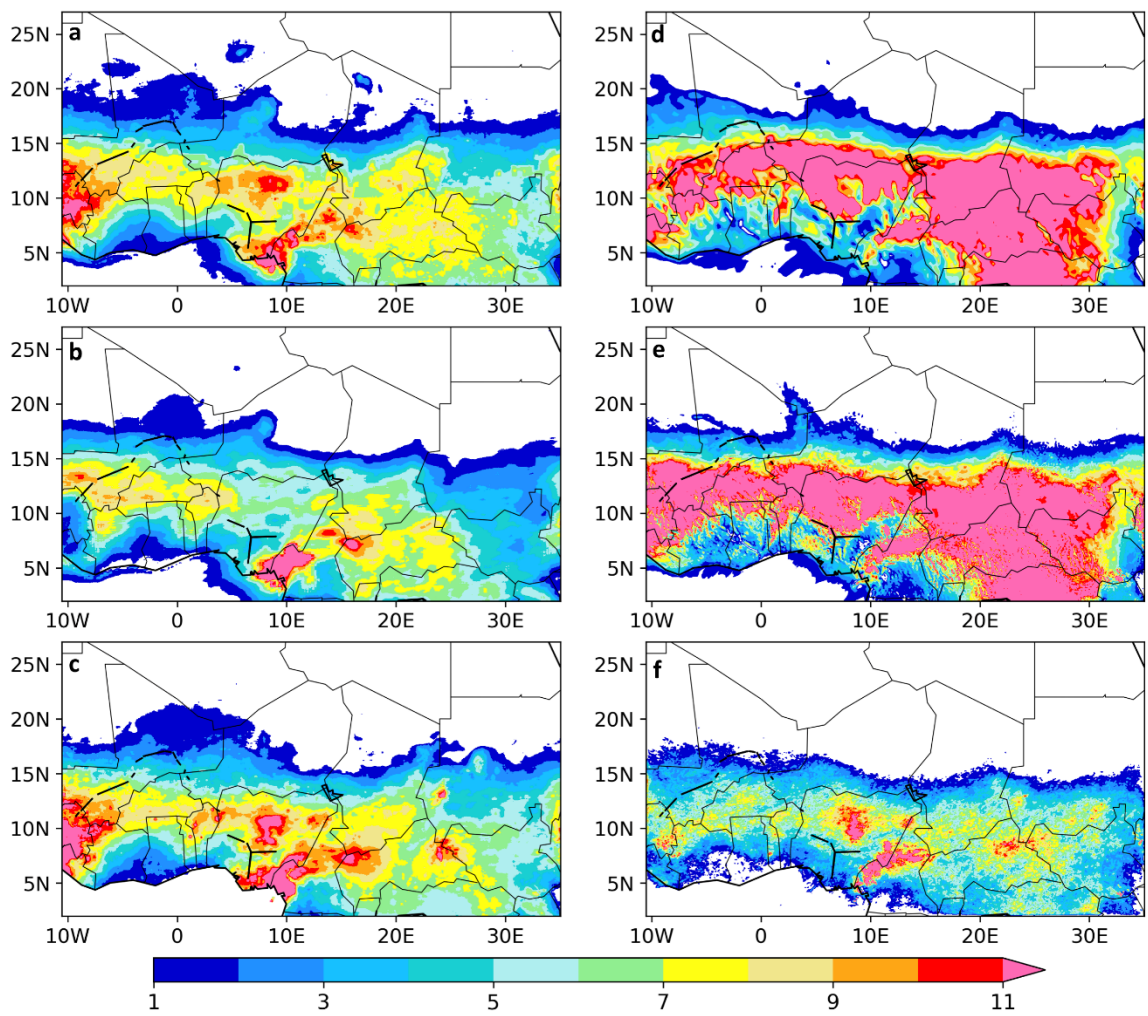


Fig.3 August mean precipitation (mm·day⁻¹) averaged over 2000 – 2019 from **a** IMERG, **b** CMORPH and **c** CHIRPS2. Ensemble mean precipitation from the **d** 27-km, **e** 9-km and **f** 3-km domains of Small-Lake simulations. The latitudinal and longitudinal ranges are from the 3-km domain.

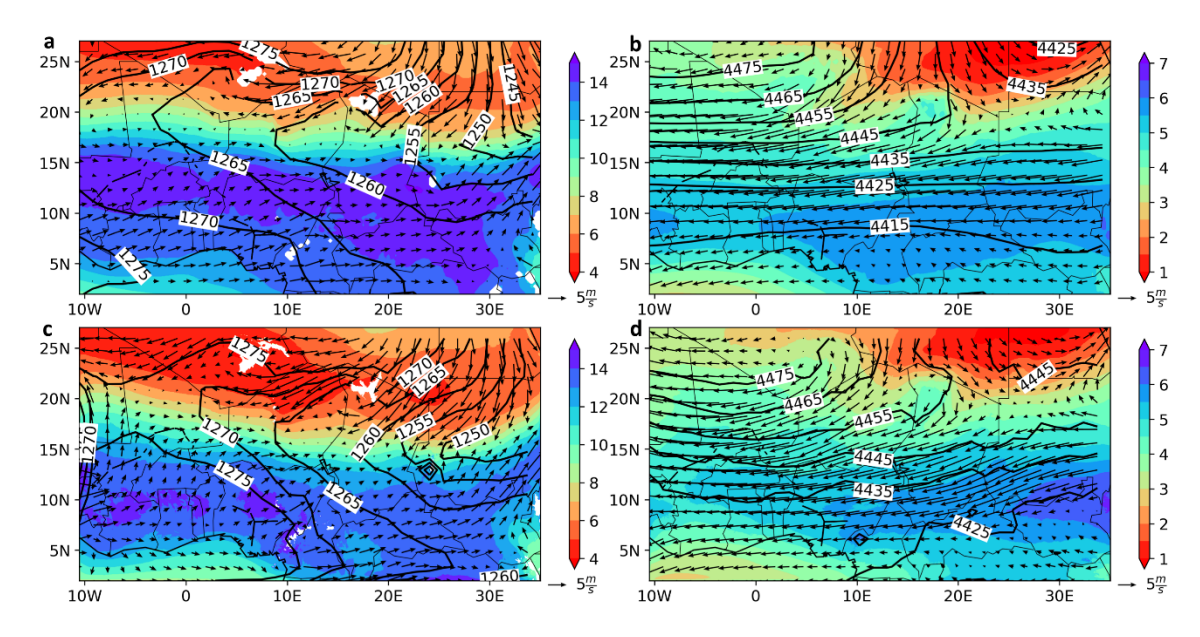


Fig.4 a 875-hPa and **b** 600-hPa specific humidity (10⁻³ kg·kg⁻¹; shading), geopotential (m²·s⁻²; contours) and horizontal wind (m·s⁻¹; vectors) in August from ERA5, averaged over 1979-2019. The contours and vectors are plotted every 6 grids for clarity. **c** 875-hPa and **d** 600-hPa specific humidity, geopotential and horizontal wind in August from the ensemble mean of Small-Lake in the 3-km domain. The contours and vectors are plotted every 50 grids for clarity

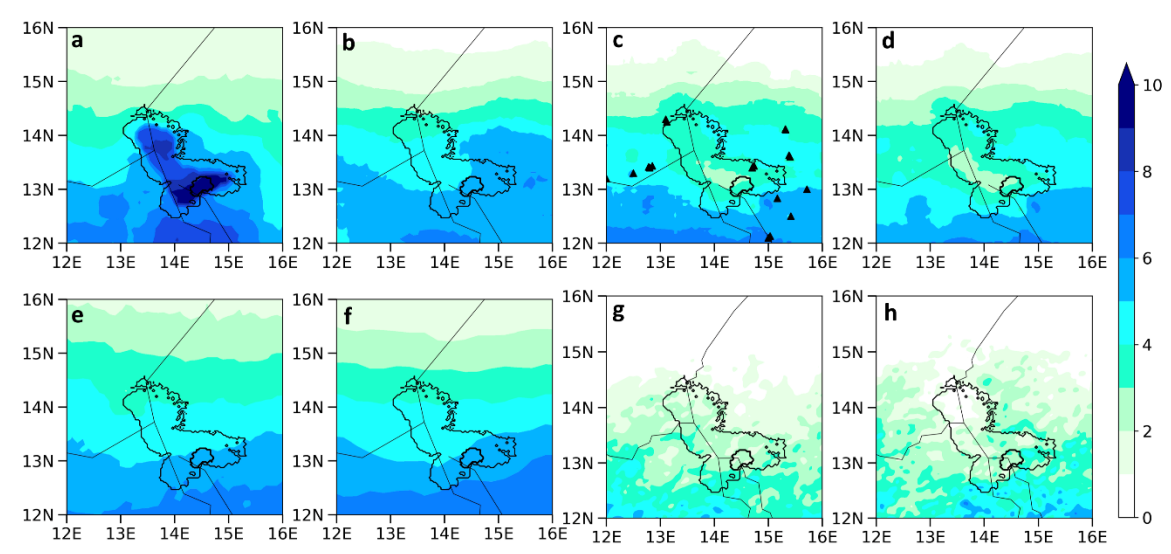


Fig.5 August mean rainfall (mm·day⁻¹) from **a** IMERG, **b** CMORPH, **c** CHIRPS2, **d** TARCAT, **e** ARC2 and **f** PERSIANN for 2000-2019. Ensemble mean rainfall from the 3-km domains of **g** Small-Lake and **h** Wetland. Black triangles denote the locations of in-situ data incorporated in CHIRPS2

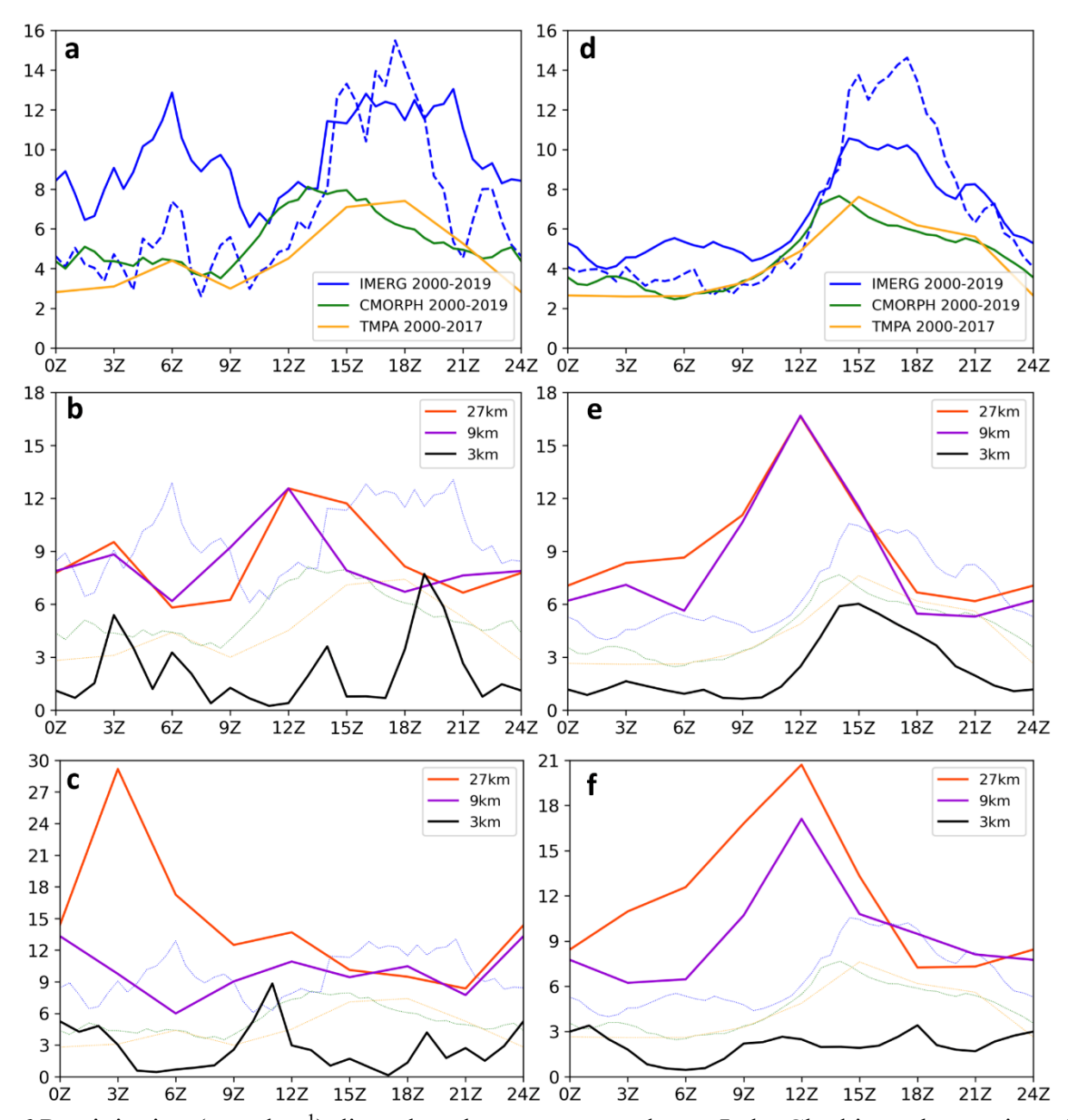


Fig.6 Precipitation (mm·day⁻¹) diurnal cycle area-averaged over Lake Chad in **a** observations, **b** Small-lake and **c** Wetland during August. Precipitation diurnal cycle over the wetlands in **d** observations, **e** Small-lake and **f** Wetland during August. The wetland area as the averaging region is stippled in Fig. 1b. The averaging regions for IMERG, CMORPH and TMPA are interpolated from the lake/wetland area in the 9-km, 9-km and 27-km domains of Small-Lake, respectively. Dashed lines represent data from the infrared-only rainfall dataset in IMERG

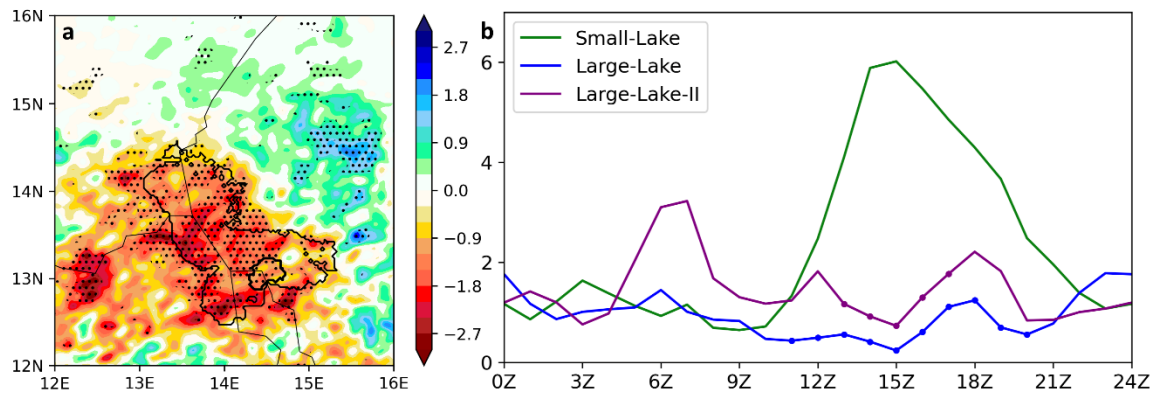


Fig.7 a Rainfall difference (mm·day⁻¹) between the Large-Lake and Small-Lake ensemble means in the 3-km domain. Values at or exceeding the 95% confidence level based on a Welch's t-test are stippled. **b** Diurnal cycle of precipitation (mm·day⁻¹) averaged over the wetland area (stippled in Fig.1b) from the Small-Lake, Large-Lake, and Large-Lake-II ensemble means. Dots denote differences between Small-Lake and the two large-lake experiments that exceed the 95% confidence level based on Welch's t-tests

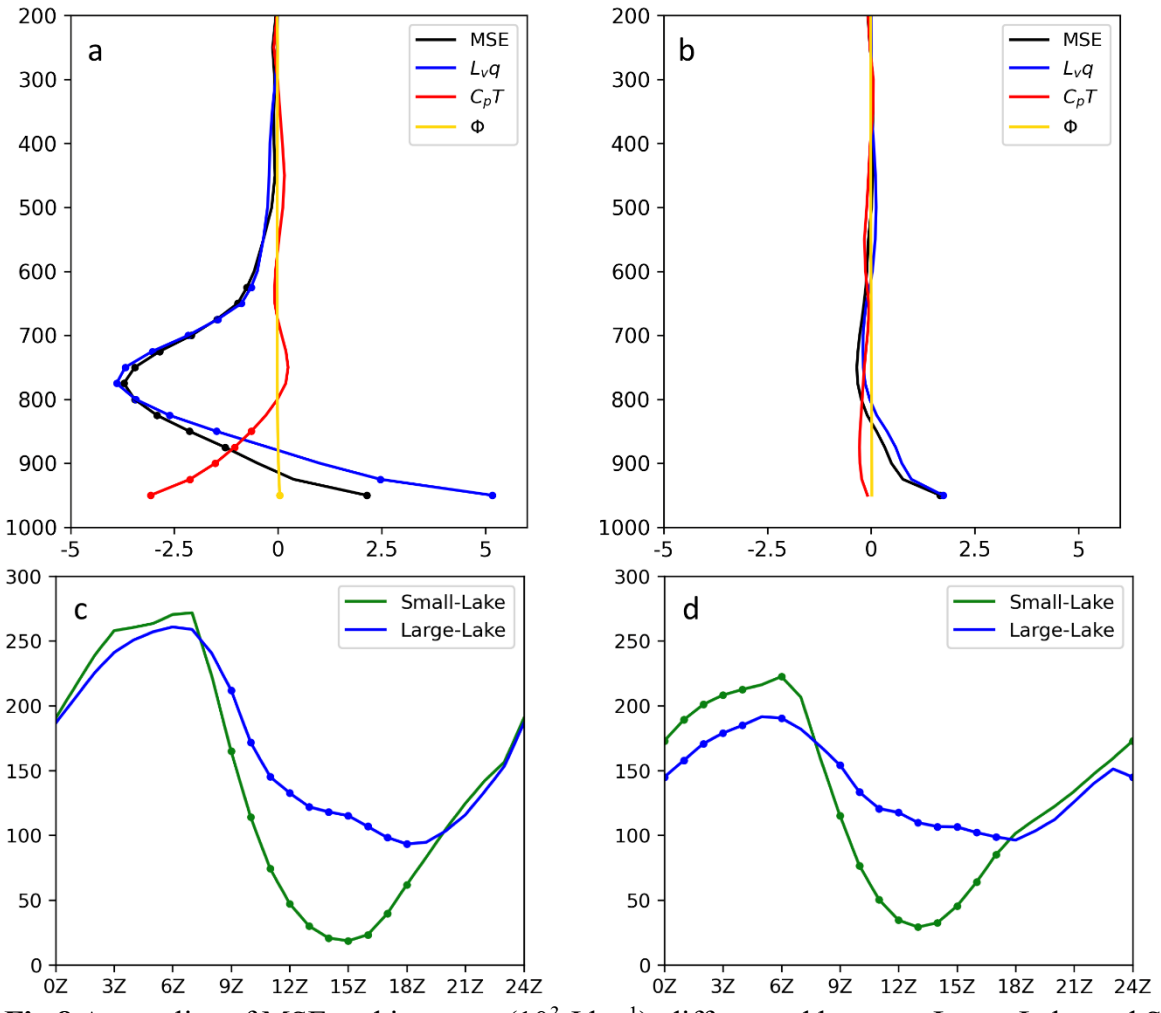


Fig.8 Anomalies of MSE and its terms (10³ J·kg⁻¹), differenced between Large-Lake and Small-Lake at **a** 15Z and **b** 00Z for the dry-hour composite averaged over the wetland area. Diurnal cycle of 950-hPa CIN in Small-Lake and Large-Lake-I for the **c** dry- and **d** rainy-day composites. Dots denote values exceeding the 95% confidence level based on Welch's t-tests

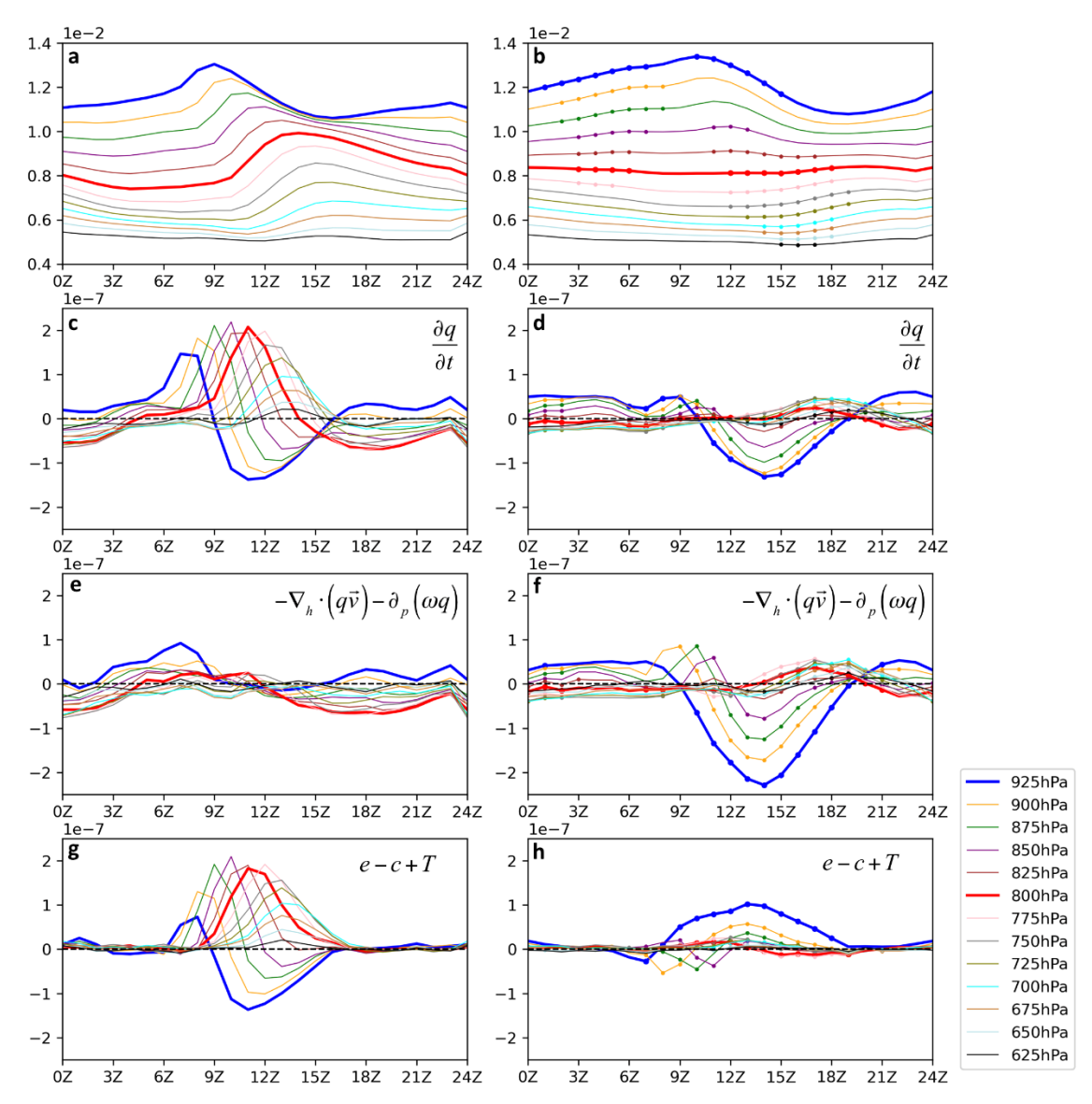


Fig.9 Diurnal cycle of specific humidity (kg·kg⁻¹) over the wetland area in **a** Small-Lake and **b** Large-Lake for the dry days composites. Diurnal cycle of the time rate change of specific humidity (s⁻¹) over the wetland area in **c** Small-Lake and **d** Large-Lake. Diurnal cycle of the moisture flux convergence (s⁻¹) over the wetland area in **e** Small-Lake and **f** Large-Lake. Diurnal cycle of the residual term (s⁻¹) over the wetland area in **g** Small-Lake and **h** Large-Lake. Dots denote differences between Small-Lake and Large-Lake that exceed the 95% confidence level based on Welch's t-tests

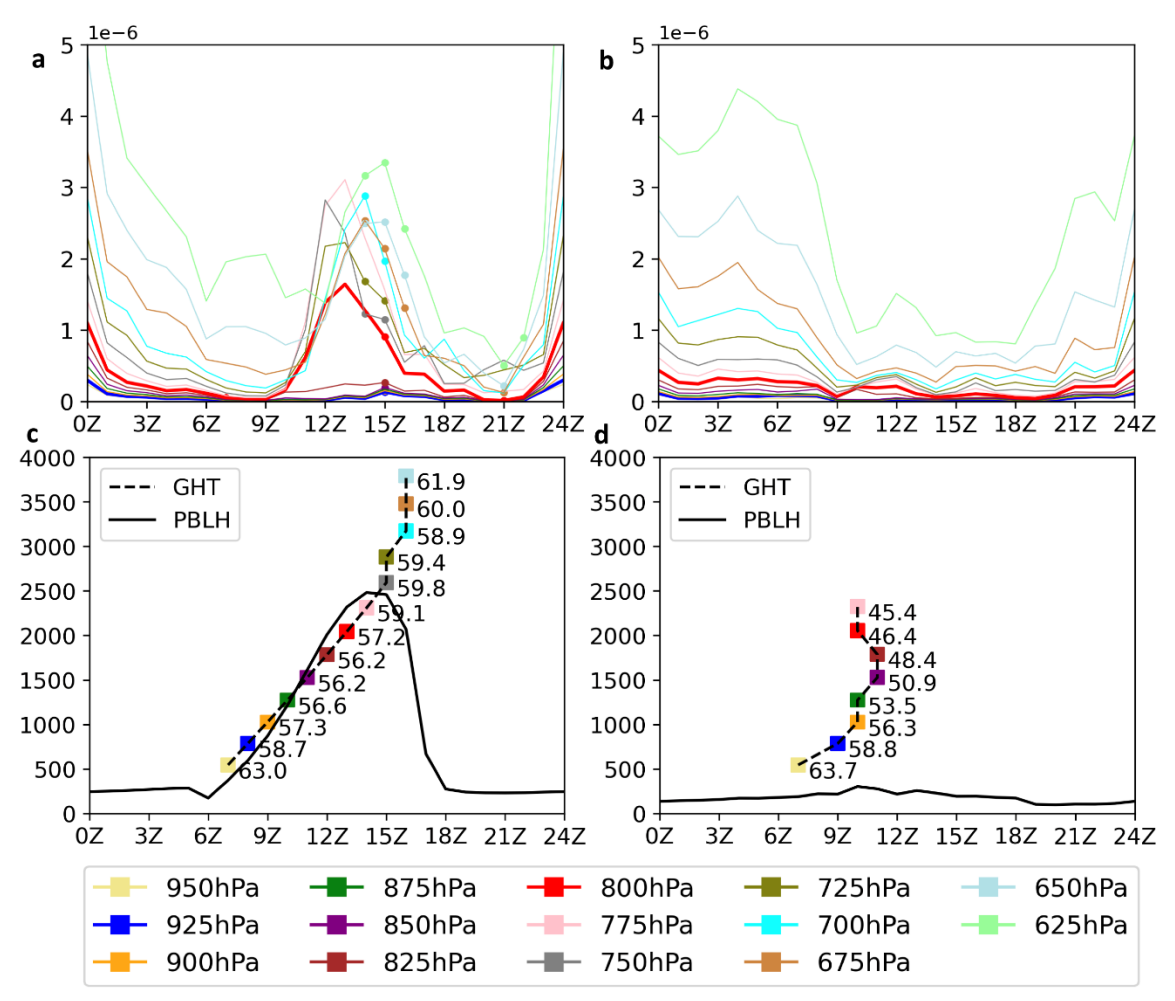


Fig.10 Diurnal cycle of water in non-gas (cloud, rain, ice, snow, and graupel) phase (kg·kg⁻¹) over the wetland area in **a** Small-Lake and **b** Large-Lake for the dry-day composite. The time and geopotential height (GHT; m) of the daytime maximum relative humidity (%; square) at 925-625 hPa, and the PBLH (m) over the wetland area in **a** Small-Lake and **b** Large-Lake for the dry-day composite. Dots denote differences between Small-Lake and Large-Lake that exceed the 95% confidence level based on a Welch's t-test

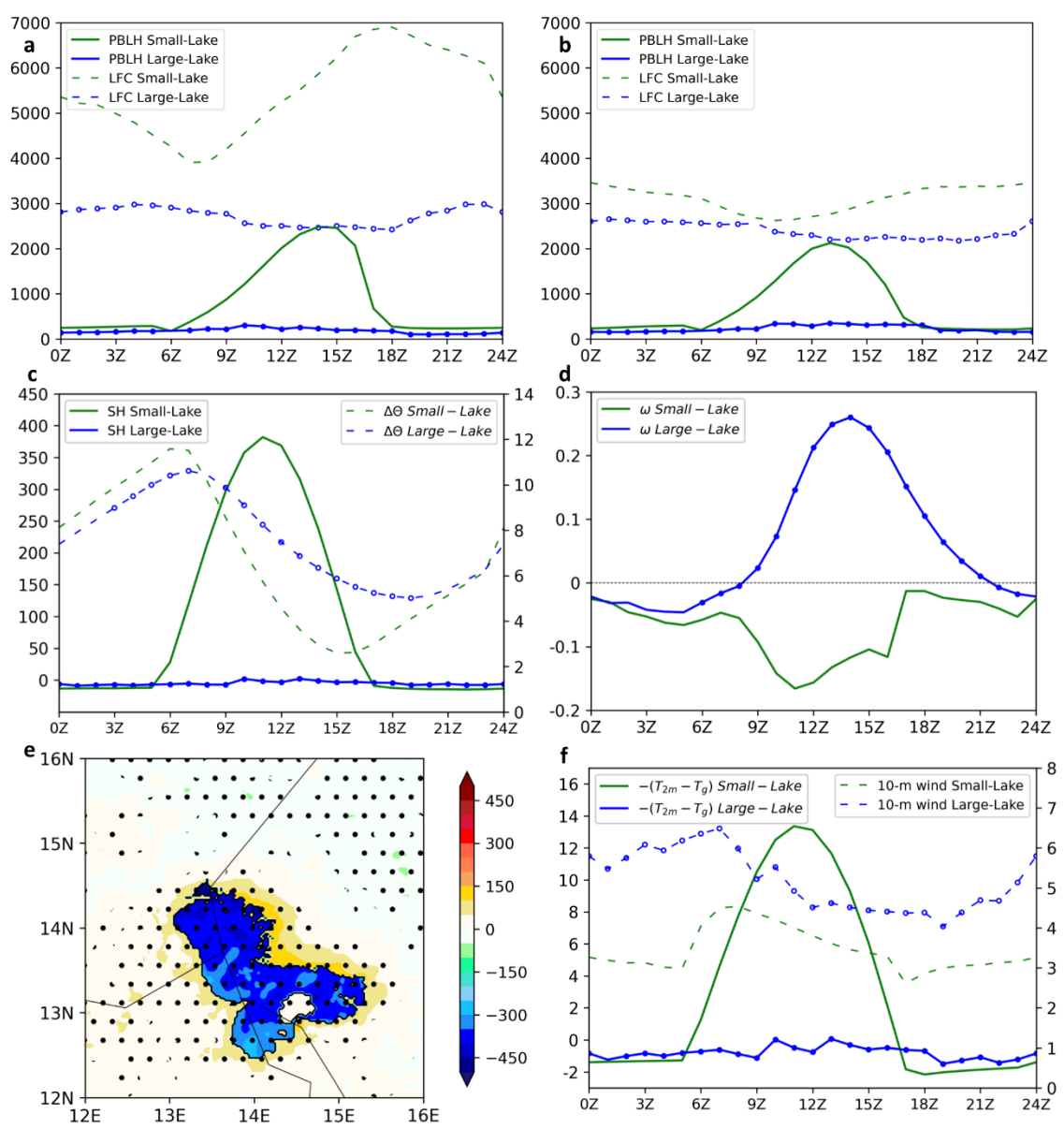


Fig.11 The planetary boundary layer height (PBLH; m; solid line) and the level of free convection (LFC; m; dashed line) in Small-Lake and Large-Lake over the wetland area, for the **a** dry- and **b** rainy-day composites. **c** Sensible heat flux (SH; W·m⁻²; solid line) and anomalous potential temperature between 700 hPa and 950 hPa ($\Delta\theta$; K; dashed line) in Small-Lake and Large-Lake over the wetland area, for the dry-day composite. **d** Vertical p-velocity at the pressure level closest to the PBLH (ω ; Pa·s⁻¹) in Small-Lake and Large-Lake over the wetland area, for the dry-day composite. **e** Differences of sensible heat flux (W·m⁻²) between the Large-Lake and Small-Lake ensemble means, for the dry-day composite. **f** Anomalies between the surface and 2 m temperatures (-(T_{2m}-T_g); K; solid line) and the 10-m wind speed (m·s⁻¹; dashed line) in Small-Lake and Large-Lake over the wetland area, for the dry-day composite. Dots denote differences between Small-Lake and Large-Lake that exceed the 95% confidence level based on Welch's t-tests

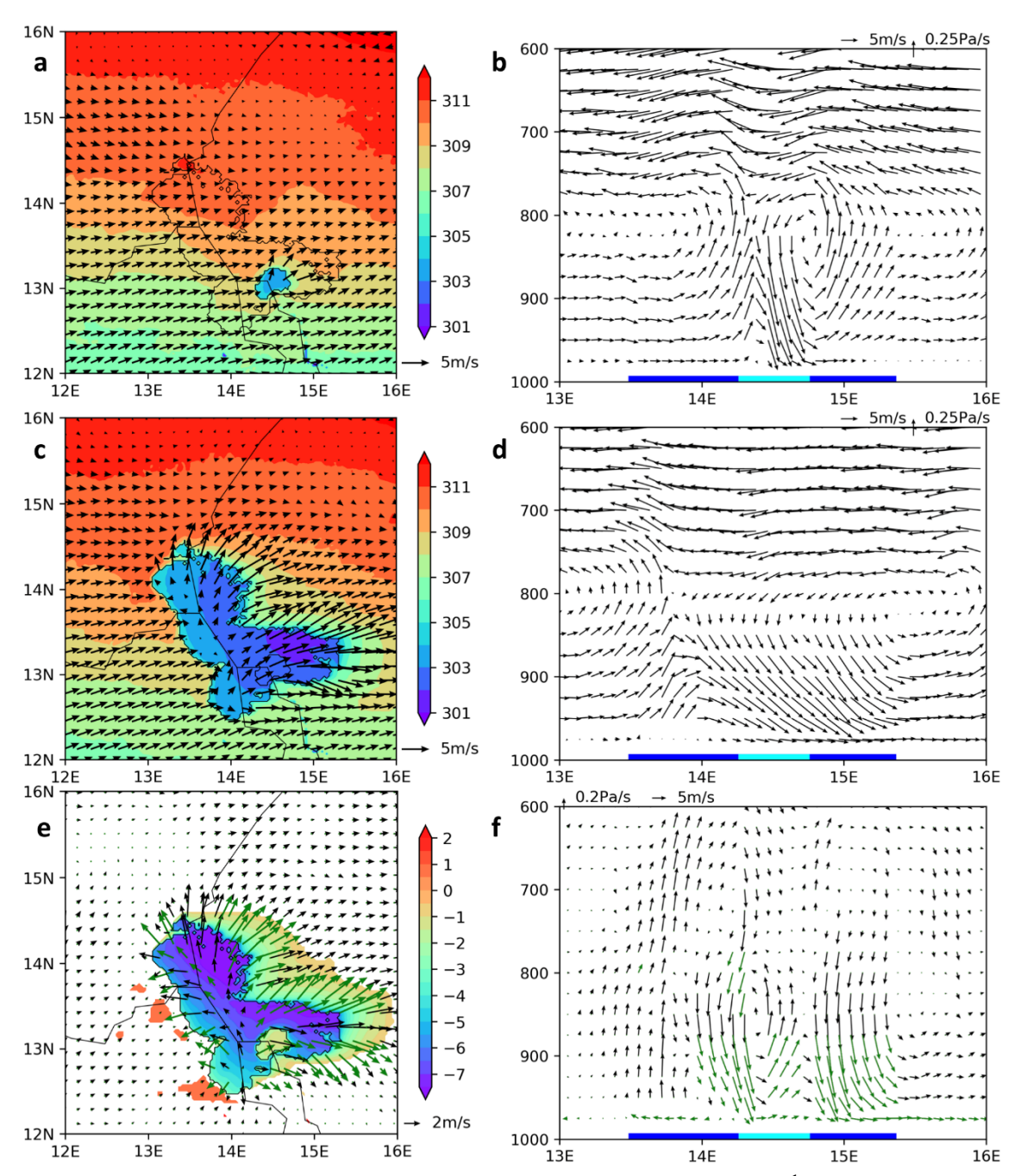


Fig.12 a 2m-temperature (K; shading) and 10-m horizontal wind (m·s⁻¹) at 12Z in Small-Lake for the dry-day composite. **b** Vertical cross sections of the zonal wind (m·s⁻¹) and vertical p-velocity (Pa·s⁻¹) at 12Z in Small-Lake for the dry-day composite averaged over the latitudes of the small lake. **c-d** are similar to **a-b**, but for Large-Lake. **e-f** are differences between Large-Lake and Small-Lake. The longitudes of the small and the large lake are marked by light and dark blue bars, respectively. Values exceeding the 95% confidence level are shown in shading or denoted by green vectors based on Welch's t-tests. Vectors are plotted every 6 grids in **a**, **c** and **e**, and every 3 grids in longitudes in the vertical cross sections for clarity

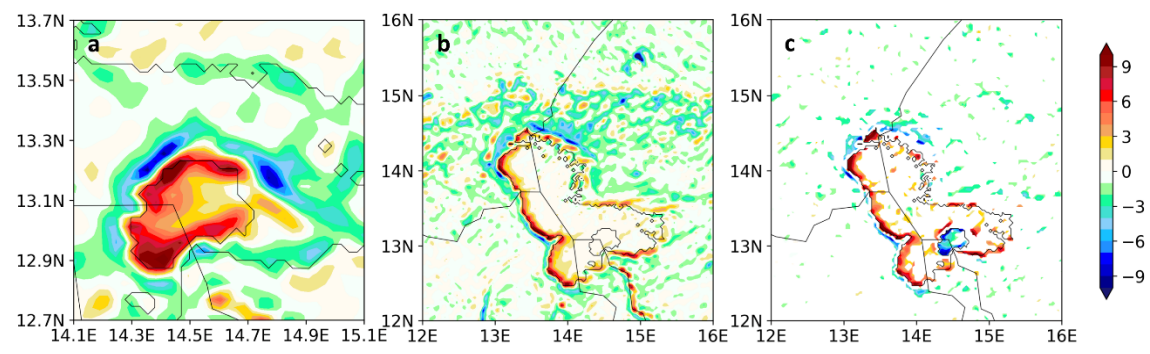


Fig.13 Material acceleration of the 875-hPa vertical p-velocity (Pa·s⁻²) at 12Z in **a** Small-Lake and **b** Large-Lake for the dry-day composite. **c** plots the differences between Large-Lake and Small-Lake. Values exceeding the 95% confidence level are shown in shading based on Welch's t-tests.

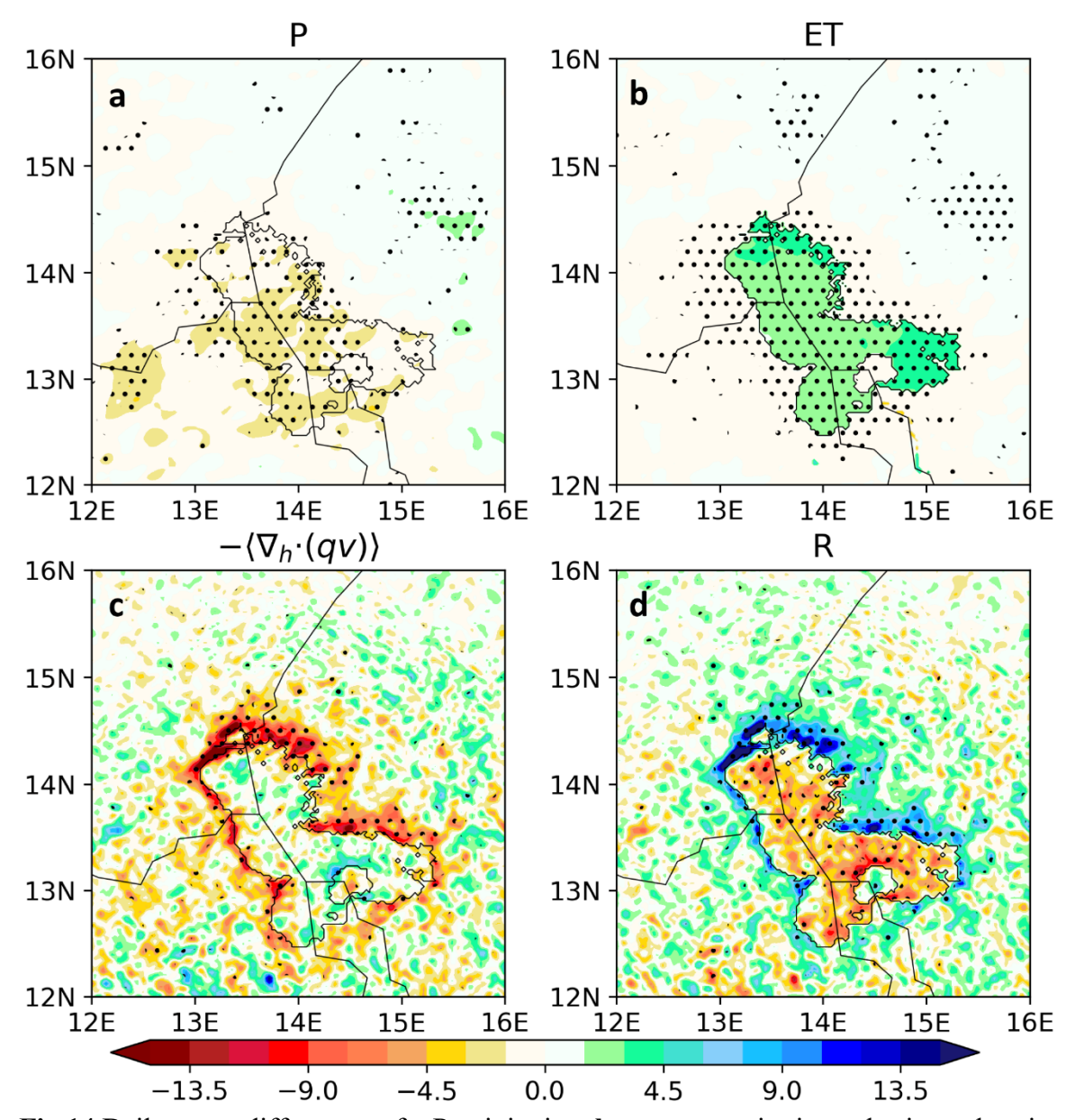


Fig.14 Daily-mean differences of **a** Precipitation, **b** evapotranspiration, **c** horizontal moisture convergence and **d** the residual term (mm·day⁻¹; Eqn. 2) between the Large-Lake and Small-Lake ensemble means. Values at or exceeding the 95% confidence level are stippled based on Welch's t-tests

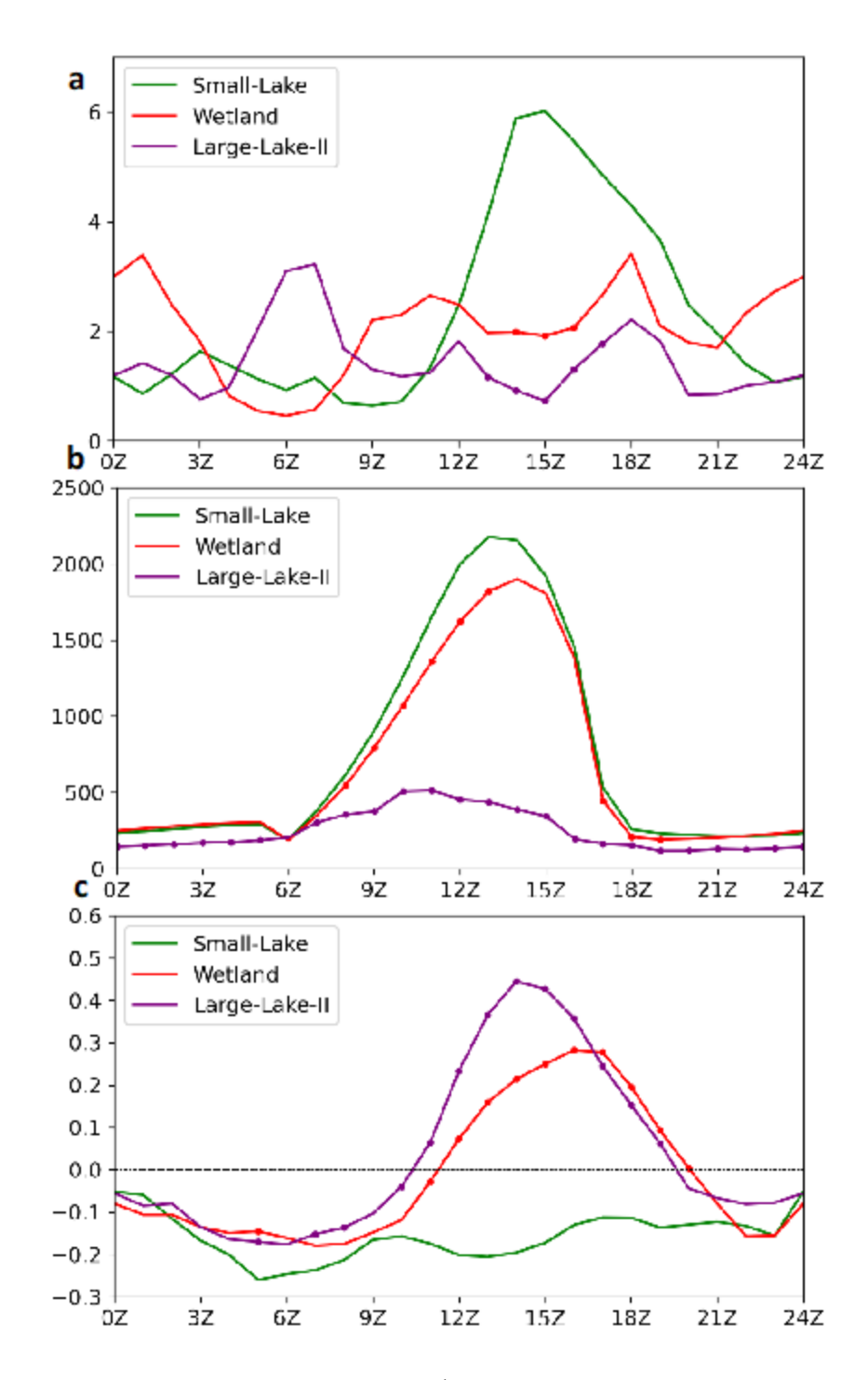


Fig.15 a Diurnal cycle of precipitation (mm·day⁻¹) over the wetland area from the Small-Lake, Large-Lake-II, and Wetland ensemble mean. **b** The PBLH (m) over the wetland area from the Small-Lake, Large-Lake-II, and Wetland ensemble mean. **c** Diurnal cycle of 825-hPa vertical pvelocity (Pa·s⁻¹) over the wetland area in Small-Lake, Large-Lake-II, and Wetland for the dryday composite. Dots denote differences between Small-Lake and the other two experiments that exceed the 95% confidence level based on Welch's t-test